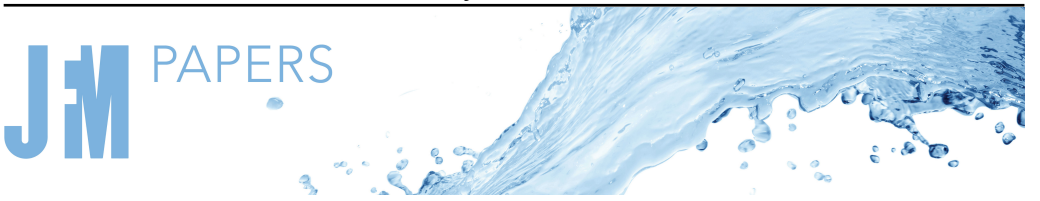
*J. Fluid Mech.* (2025), *vol.* 1024, A17, doi:10.1017/jfm.2025.10797



# Control and scaling of flow separation from a curved ramp using a pulsed jet

**Shengtai He**[1] **and Yu Zhou**[2,3]

[1]Centre for Turbulence Control, Harbin Institute of Technology (Shenzhen), Shenzhen 518055, PR China

[2]School of Mechanical Engineering & Mechanics, College of Engineering, Eastern Institute of Technology, Ningbo 315000, PR China

[3]Ningbo Key Laboratory of Advanced Manufacturing Simulation, Eastern Institute of Technology, Ningbo 315000, PR China

**Corresponding authors:** Yu Zhou, yuzhou@eitech.edu.cn; Shengtai He, heshengtai_fluid@163.com

(Received 21 January 2025; revised 29 August 2025; accepted 26 September 2025)

An experimental study is performed to control flow separation from a two-dimensional curved ramp using a spanwise pulsed blowing slit jet placed near the separation point of the baseline flow. The momentum-thickness-based Reynolds number $Re_\theta$ is 5700. Four control parameters are investigated, including the velocity ratio $\overline{U^*_{J,c}}$, duty cycle $dc$, dimensionless excitation frequency $f_e^*$ and jet blowing angle $\alpha$. The control mechanisms are found to differ from small to large jet angle. Empirical scaling analysis for $\alpha \leq 55°$ unveils that $\Delta\overline{C_{p,e}} = f_1(\overline{U^*_{J,c}}, dc, f_e^*, \alpha, Re_\theta)$ may be reduced to $\Delta\overline{C_{p,e}}/\Pi(\tau) = f_2(\xi)$, where $f_1$ and $f_2$ are different functions, $\Delta\overline{C_{p,e}}$ is the variation in the pressure coefficient at the end of the ramp under control, $\Pi(\tau)$ is a function of dimensionless duration $\tau$ at which the jet is closed within one excitation period, $\Delta\overline{C_{p,e}}/\Pi(\tau)$ represents the control efficiency, and $\xi$ is a scaling factor that is physically the energy ratio per unit area of the blowing jet to the mainstream. This scaling law is also found to be valid for steady jet control. Several interesting inferences can be made from this scaling law, which provides important insight into the physics of flow separation control.

**Key words:** boundary layer control, boundary layer separation, drag reduction

## 1. Introduction

Turbulent flow over a backward-facing curved ramp or a curved ramp for simplicity is associated with an adverse pressure gradient (APG) turbulent boundary layer (TBL) and may separate, as frequently seen in engineering applications such as aircraft wings, land and underwater vehicles, turbomachines, combustors, and diffusers. The flow separation

© The Author(s), 2025. Published by Cambridge University Press.



https://doi.org/10.1017/jfm.2025.10797 Published online by Cambridge University Press

may adversely affect the performance of these devices. For instance, flow separation in the wake of an underwater vehicle will significantly increase its drag and noise. As such, this flow and its separation control have attracted much interest in the turbulence community.

Flow separation from a curved ramp is extensively investigated both experimentally and numerically. Previous studies provide valuable insight into the physics of this flow, which may be divided into five stages, i.e. flow acceleration, deceleration, separation, reattachment and downstream recovery. The favourable pressure gradient region induced by the wall curvature effect causes the boundary layer to thin and accelerate at the upstream of the curved ramp (Eaton & Song 2004; Asgari & Tadjfar 2016). The TBL thickness in the APG region grows rapidly and begins to decelerate. Right before flow separation, the mean velocity profile becomes inflectional and develops an inflection point (Song & Eaton 2002; El-Askary 2009; Lardeau & Leschziner 2011). Unlike flow separation from a fixed point, e.g. backward-facing step and backward-facing ramp, the separation point oscillates randomly over the ramp surface. Both separation and reattachment are intermittent and highly unsteady for the curved ramp flow (Bentaleb, Lardeau & Leschziner 2012). The probability density functions of the separation and reattachment points display Gaussian and plateau-like distributions, respectively (He *et al.* 2023), and depend strongly on the momentum-thickness-based Reynolds number $Re_\theta$ (Song & Eaton 2004). With increasing $Re_\theta$, flow separation is postponed but the reattachment point shifts slightly upstream, though both become independent of $Re_\theta$ once $Re_\theta \geq 5700$ (He *et al.* 2023). In the separated shear layer, the Kelvin–Helmholtz instability produces roller vortices, which flap up and down, generating a high turbulence kinetic region above the separation bubble. Inside the bubble, all Reynold stress components and turbulent kinetic energy are relatively small (Song, Degraa & Eaton 2000). The flapping motion is probably also associated with the slow growth and contraction of the separation bubble (Song & Eaton 2004; EI Askary 2009).

Both passive and active control techniques have been developed to suppress flow separation from the curved ramp. The former requires no external power input. For example, vortex generators may create streamwise vortices and hence enhance mixing between the low-momentum flow in the near-wall boundary layer and high-momentum mainstream, thus suppressing flow separation and achieving substantial pressure recovery (e.g. Duriez, Aider & Wesfreid 2008; Koklu & Owens 2017). Other techniques have also been proposed, including the surface-mounted fence (Neumann *et al.* 2004), convergent-divergent (C-D) riblets (Guo, Zhong & Craft 2020) and micro bumps (Gorton, Jenkins & Anders 2002). In spite of their great success in controlling flow separation, passive devices are characterised by permanent fixtures which are not readily modified or removed and may generate a parasitic drag. Furthermore, their control performance may deteriorate when departing from the design conditions.

Active techniques are characterised by a strong manipulation ability, great design flexibility and easy adjustability, and thus may potentially achieve excellent control performance across a wide range of operating conditions. Synthetic jets have been applied for controlling flow separation from the curved ramps. Zhang & Zhong (2010, 2011) and Zhong & Zhang (2013) deployed round-hole synthetic jets, which injected the momentum into the mainstream and interacted with the TBL to generate hairpin vortices. These vortices induced one pair of counter-rotating streamwise vortices near the wall, producing a downwash bringing the high-momentum fluid towards the wall and hence reducing flow separation. Lardeau & Leschziner (2011) used similar jets to cut down the separation bubble size by 20 % at $Re_\theta = 1160$. In contrast, synthetic jets through slits enhance momentum transfer via approximately two-dimensional spanwise vortices (Asgari & Tadifar 2019). Asgari & Tadifar (2022) examined the role played by a phase difference between two adjacent synthetic jets and concluded that a $\pi/2$ lead by the upstream jet



https://doi.org/10.1017/jfm.2025.10797 Published online by Cambridge University Press

was most efficient, causing the separation bubble size to contract by approximately 40 % and, meanwhile, the wall pressure fluctuation to diminish at $Re_\theta = 1200$. Also using slit synthetic jets, Dandois, Garnier & Sagaut (2007) demonstrated numerically that the separation bubble could be reduced by 54 % at $Re_\theta = 1410$. Leschziner & Lardeau (2011) advocated that, if properly configured, slit synthetic jets could be more effective than round-hole ones and have a better spanwise uniformity. Nevertheless, synthetic jets must be able to generate an adequately large exit velocity to produce strong vortices should they be effective for flow separation control (Gorton *et al.* 2002). Selby, Lin & Howard (1992) deployed one spanwise array of round-hole jets, referred to as vortex generator jets (VGJs), to suppress flow separation from a curved ramp. They performed a parametric study of VGJs, including the jet position, speed, orientation, orifice diameter and spacing. The blowing angles $\beta$ of adjacent jets differed alternately between $+90°$ and $-90°$ to produce counter- or co-rotating streamwise vortices. It was noted that the counter-rotating vortices were not so effective as the co-rotating ones. These vortices intensified the momentum transfer, thus suppressing flow separation and achieving pressure recovery. Razzaghi *et al.* (2022) investigated, at $Re_\theta = 2800$, the effect of the jet position and orifice spacing on the control performance, and obtained a maximum contraction in the separation bubble size by 78 %. Other control methods have also been proposed, including the sweeping jet (Koklu *et al.* 2017), oscillating blowing jet (Neumann *et al.* 2004) and plasma (Rizzetta *et al.* 2010).

Previous studies have improved tremendously our understanding of the control of flow separation from the curved ramp. Nevertheless, several important issues remain to be addressed. First, the techniques reported are mostly based on the mechanism of momentum transfer, achieving a rather limited success. In their attempt to control flow separation from aerofoils, Pfingsten & Radespiel (2009), Nishino, Hahn & Shariff (2010) and Xu *et al.* (2018) managed to eliminate flow separation using a tangential steady or unsteady blowing slit jet, which induced the Coanda effect. Compared with a steady jet, the unsteady jet can massively reduce the required mass flow rate (Sellers, Jones & Moore 2002; Liu *et al.* 2004; Jones *et al.* 2010; El Sayed *et al.* 2017). However, a systematic study has yet to be conducted to suppress flow separation from a curved ramp using an unsteady blowing jet. For example, the blowing angle effect on the control performance has not been thoroughly understood. Second, previous studies on suppressing flow separation from a curved ramp were mostly carried out at rather low Reynolds numbers ($Re_\theta < 3000$) although most relevant engineering applications involve much higher Reynolds numbers; there is a lack of higher Reynolds number data. Third, flow separation control may depend on many parameters, e.g. the mass flow rate, excitation frequency, duty cycle and blowing angle under unsteady blowing, which makes the control problem highly sophisticated. Can we reduce these parameters into a single one, that is, find a scaling factor that governs the control performance and reflects the essence of the flow physics under control? The success in resolving this issue may provide important physical insight into the inter-relationships between the control parameters and may even have a profound impact upon possible practical applications since the flow structure and the similarity parameter obtained from a laboratory-scale model are the same as those of a full-scale model (Perumal & Zhou 2018; Haffner *et al.* 2020; Perumal *et al.* 2022).

This work sets out to address the above-mentioned issues through quite extensive experiments and careful analysis of experimental data. The control of flow separation from a curved ramp is investigated using an unsteady blowing jet through a spanwise slit at $Re_\theta = 5700$. The remainder of this paper is organised as follows. Experimental details are given in § 2. The control jet characteristics and incoming flow TBL are documented in § 3. The systematic parametric study and control mechanisms are discussed in § 4.



https://doi.org/10.1017/jfm.2025.10797 Published online by Cambridge University Press

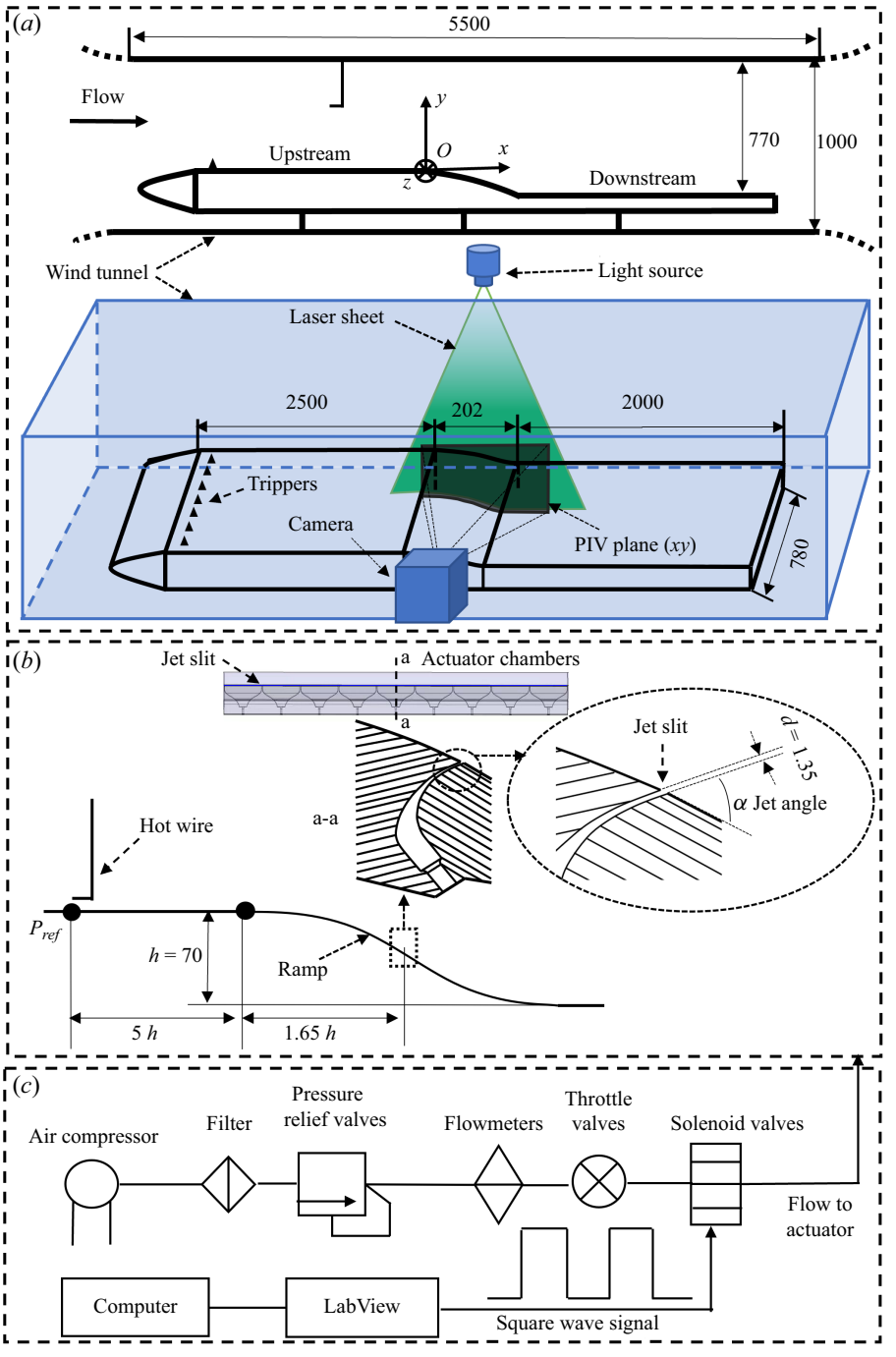



Figure 1. (*a*) Experimental set-up along with the definition of the coordinate system; (*b*) ramp and actuator where the blowing angle may be adjusted by replacing the 3-D-printed curved surface; (*c*) system to produce a pulsed and controllable blowing jet. Dimensions are not to scale and the units are in mm.



https://doi.org/10.1017/jfm.2025.10797 Published online by Cambridge University Press

The empirical scaling analysis is presented in § 5, and net energy saving and control efficiency in § 6. This work is concluded in § 7.

## 2. Experimental details

### 2.1. *Experimental set-up*

Experiments are carried out in a closed-circuit wind tunnel with a test section with dimensions of 5.5 m long, 1 m high and 0.8 m wide. The non-uniformity of the flow in the test section is approximately 0.1 % and the longitudinal turbulence intensity is less than 0.4 % for the wind speed range involved. Figure 1(*a*) presents a schematic of the experimental set-up. The test rig includes five major components, the leading edge, trippers, an upstream plate, a curved ramp and a downstream plate. The rig is placed horizontally on the bottom wall of the test section and spans the entire tunnel width. The leading edge is shaped to the NACA0015 aerofoil profile to avoid flow separation. Following Bai *et al.* (2014) and Cheng *et al.* (2021), the flow is tripped using one spanwise array of screws, placed at 0.1 m downstream of the leading edge, which acts to perturb incoming flow, accelerating the formation of the fully developed TBL over the upstream plate. Due to the presence of an APG associated with the ramp, the TBL separates from the curved ramp and then reattaches on the downstream plate. The right-handed Cartesian coordinate system is defined such that its origin $O$ is at the midpoint of the upper edge of the ramp and the coordinates $x$, $y$ and $z$ are along the streamwise, vertical and spanwise directions, respectively. We use $U$, $V$ and $W$ to represent the instantaneous velocity components in the $x$, $y$ and $z$ directions, respectively, which can be decomposed as $U = \overline{U} + u$, $V = \overline{V} + v$ and $W = \overline{W} + w$, where the overbar denotes time-averaging, and $u$, $v$ and $w$ are the fluctuating components. Hereinafter, the superscript asterisk '$*$' denotes normalisation by the ramp height $h$ and/or the free stream velocity $U_\infty$, and bracket '$\langle\ \rangle$' denotes phase-averaging based on the period of the pulsed jet. The $h$ and longitudinal length of the curved ramp are 70 and 202 mm, respectively. The ramp consists of two circular arcs with radii of 282 and 141 mm. Readers should refer to Lardeau & Leschziner (2011) for more details, such as the mathematical equations of the curves, regarding the curved ramp model. The expansion ratio of the heights downstream of the ramp to that upstream is 1.1, which is sufficiently small to avoid the interference effect of the wind tunnel (Song *et al.* 2000; Zhang & Zhong 2010; Lim *et al.* 2021). The width-to-height ratio of the ramp is 11.2, larger than the critical value of 10 to ensure the two-dimensionality of the baseline flow (Park *et al.* 2007; Ma & Schroder 2017; Li *et al.* 2020), thus ensuring negligible three-dimensional effects from the side walls of the test section. This is confirmed by the measured spanwise distribution of the time-averaged pressure coefficient ($\overline{C_p}$) on the ramp (Stella, Mazellier & Kourta 2017), which is constant for $z^* = -4$ to 4 within experimental uncertainties.

Figure 1(*c*) shows the pressurised air supply and regulation system. The airflow from the air compressor is filtered and dried through the air filter, and is then stabilised and adjusted in pressure via a high-precision pressure relief valve (SMC IR3020). Ideally, given a fixed supply pressure, the mass flow rate should be independent of the excitation frequency $f_e^*$ and proportional to the duty cycle $dc$. However, the mass flow rate will vary with $f_e^*$ due to the mechanical limitation of solenoid valves (Jones *et al.* 2002; Wong *et al.* 2007; Joseph *et al.* 2013). Thus, to control the mass flow rate and $f_e^*$ independently, we use a flowmeter (MF4008-50-08-BV-A) and throttle valve to display and change the mass flow rate, respectively. The $f_e^*$ and $dc$ are independently controlled using a National Instruments (NI) system via nine solenoid valves (FESTO MHJ10-S-2.5-QS-4-MF), whose use ensures



https://doi.org/10.1017/jfm.2025.10797 Published online by Cambridge University Press

the reasonably spanwise uniformity of the slit jet (figure 1*b*). The *dc* is a fraction of the duration, during which the solenoid valve is opened, and varies from 0.3 to 0.9. The maximum operating frequency of the valve is 300 Hz. Finally, the air is injected through a spanwise slit located at $x^* = 1.65$ (figure 1*b*), slightly upstream of the flow separation point $\overline{x_s^*} = 1.7$ given $Re_\theta \geq 5700$, with a width of $d = 1.35$ mm. The blowing jet angle $\alpha$, defined as the angle between the blowing jet and the tangential line of the local ramp surface, can be changed by replacing the 3-D-printed ramp. There are altogether six different ramps so that $\alpha$ may vary from 0° (local tangential direction) to 115° (vertical direction). All pneumatic components are connected via simi-rigid tubes with a diameter of 8 mm.

### 2.2. *Flow measurements*

The $U_\infty$ is measured using a pitot tube connected to an anemometer (FC Furness Controls FCO560). A single tungsten wire with a diameter of 5 μm and 1.25 mm in length mounted on a computer-controlled Dantec traverse system is used to measure the boundary layer velocity profiles and jet outlet characteristics. The wire is operated on a constant temperature circuit (Dantec Streamline) at an overheat ratio of 1.8. The signal from the wire is offset, amplified and low-pass filtered at a cutoff frequency of 1.0 kHz, and then digitised at a sampling frequency of 3.0 kHz using a 16-bit A/D converter (NI PCI-6143). The duration of sampling is 120 s and each record of signal yields $3.6 \times 10^5$ data points.

A LaVision planar particle image velocimetry (PIV) system, placed outside the wind tunnel, is used to measure the velocity field in the ($x$, $y$) plane. The flow is seeded with paraffin-oil-generated fog, with particles of ∼1 μm in diameter. Flow illumination is provided by two standard pulsed laser sources (Vlite-200) of 532 nm in wavelength, each with a maximum energy output of 200 mJ per pulse. Each laser pulse lasts for 100 ns. One charge-coupled device (CCD) camera (Imager pro HS4M, 4-megapixel sensors, 2016 × 2016 pixels resolution) is used to capture particle images. Synchronisation between image taking and flow illumination is provided by the LaVision timer box. The time intervals between two successive pulses are 30–90 μs at varied Reynolds numbers to guarantee approximately a 4 pixels distance between two frames. The PIV-measured field of view is 210 mm × 210 mm. In processing the PIV images, the adaptive PIV method is used with a minimum interrogation area of 32 × 32 pixels and a maximum size of 64 × 64 pixels. The grid step size of 16 × 16 pixels produced 126 × 126 in-plane velocity vectors. A total of 2100 images is captured for each case, with a trigger rate of 15 Hz in the double frame mode. The uncertainties of measured $U$ and $V$ are estimated based on image matching analysis (Sciacchitano, Wieneke & Scarano 2013; Zhang *et al.* 2018) to be ∼2 % of $U_\infty$.

It is difficult to determine precisely $\overline{x_s^*}$ from the PIV measurement. The separation bubble becomes very thin near the separation point (Lardeau & Leschziner 2011). The near-wall velocity cannot be accurately calculated due to relatively large laser reflections from the wall and the spatial resolution of the PIV measurement. The $\overline{x_s^*}$, identified by the location where $\overline{U}$ changes its direction, may deviate significantly from the actual separation position. In the present work, we use the PIV data to determine an approximate range of $\overline{x_s^*}$. Then, an in-house built micro-PIV system is employed to determine the precise flow separation point. The camera of the system is fitted with a long-distance microscope lens (Model K2) and two zoom lenses with a magnification factor of 2 so that the field of view is as small as 8 mm × 8 mm. The laser sheet is adjusted to minimise its width and thickness, thus increasing the light intensity and decreasing the reflection of the wall. The particle density in the flow field is also increased to meet the requirement of cross-correlation calculation. The spatial resolution is 252 pixels mm$^{-1}$ for the micro-PIV (cf. approximately 10 pixels mm$^{-1}$ for the conventional PIV). The micro-PIV technique



https://doi.org/10.1017/jfm.2025.10797 Published online by Cambridge University Press

improves the measurement accuracy for the estimate of $\overline{x_s^*}$. The estimated uncertainty of $\overline{x_s^*}$ is less than 0.5 %.

The surface pressure on the test model is measured using a PSI DTC Initium system. The pressure taps are connected to an electronic pressure scanner via plastic tubes with an inner diameter of 1 mm. The scanner is placed inside the cavity beneath the ramp surface to minimise the length of the tubes and hence the filtering effect of tubing in pressure measurements (Zhang *et al.* 2018). The pressure coefficient $C_p$ is given by

$$C_p = \frac{P - P_\infty}{0.5\rho U_\infty^2}, \tag{2.1}$$

where $\rho$ is the air density, and $P$ and $P_\infty$ are the local and free stream static pressures, respectively. The sampling frequency is 650 Hz and a total of 40 000 data points are obtained for each measurement point. The measurement uncertainty is estimated to be $\pm$ 2 Pa. At least three runs are conducted for each measurement.

Experiments are conducted at $Re_\theta = 5700$ because the flow separation point becomes independent of $Re_\theta$ and fixed at $\overline{x_s^*} = 1.7$ (He *et al.* 2023) once $Re_\theta \geq 5700$. Four control parameters are examined, i.e. $\overline{U_{J,c}^*}$ (0.21–1.22), $dc$ (0.3–0.9), $f_e^*$(0.039–2.33) and $\alpha$ (0°–115°). Approximately 1500 cases are investigated, each involving a different set of control parameters.

## 3. Control jet and incoming boundary layer

The control jet and incoming boundary layer are first documented before the study of flow separation control. As shown in figure 2(*a*), the jet velocity $U_J$ is measured at 1 mm downstream of the slit exit in the absence of incoming flow. The spanwise variation in the time-averaged jet velocity $\overline{U_{J,c}}$ at the slit centre ($x' = 0$) is less than 5 % (figure 2*b*), indicating a reasonable spanwise uniformity of the jet.

Figure 2(*c*) shows the time history of $U_{J,c}$ at different $dc$. Given $f_e^* = 0.08$ and $\overline{U_{J,c}^*} = 0.84$, which correspond to a specified jet mass flow rate, three duty cycles are examined, i.e. $dc = 0.4$, 0.6 and 0.8. As expected, a smaller $dc$ corresponds to a larger maximum jet velocity and a shorter duration in one period. At a low frequency such as $f_e^* = 0.08$, $U_{J,c}$ exhibits the characteristics of a square wave.

Following New, Lim & Luo (2006), the jet velocity $\overline{U_J}$ is normalised by $\overline{U_{J,c}}$. Then, $\overline{U_J}/\overline{U_{J,c}}$ (figure 2*d*) collapses reasonably well about a parabolic curve, *viz.*

$$\frac{\overline{U_J}}{\overline{U_{J,c}}} = 1 - \left(\frac{x'}{x_0'}\right)^2. \tag{3.1}$$

The $\pm x_0'$ are the positions where $\overline{U_J} = 0$. This result is important to determine experimentally the jet energy. To calculate the jet energy, it is necessary to integrate spatially the jet velocity profile. When there are a large number of cases, say over 1000 in this study, it is difficult to measure the jet velocity profile for every case. Yet with (3.1), it is only necessary to measure $\overline{U_{J,c}}$ to obtain the jet velocity profile (Cheng *et al.* 2021; Zhang *et al.* 2022).

The ideal performance of a pulsed jet is that the jet velocity and frequency are independent of each other; for example, the jet mean velocity or its transient maximum remains unchanged when $f_e^*$ varies. However, this is very difficult experimentally due to the limitation of the current state-of-the-art technology of solenoid valves and the inertia of the air in the tube. Furthermore, the length from the solenoid valve to the slit exit may have an important impact upon the pulsed jet velocity and a minimised length is greatly



https://doi.org/10.1017/jfm.2025.10797 Published online by Cambridge University Press

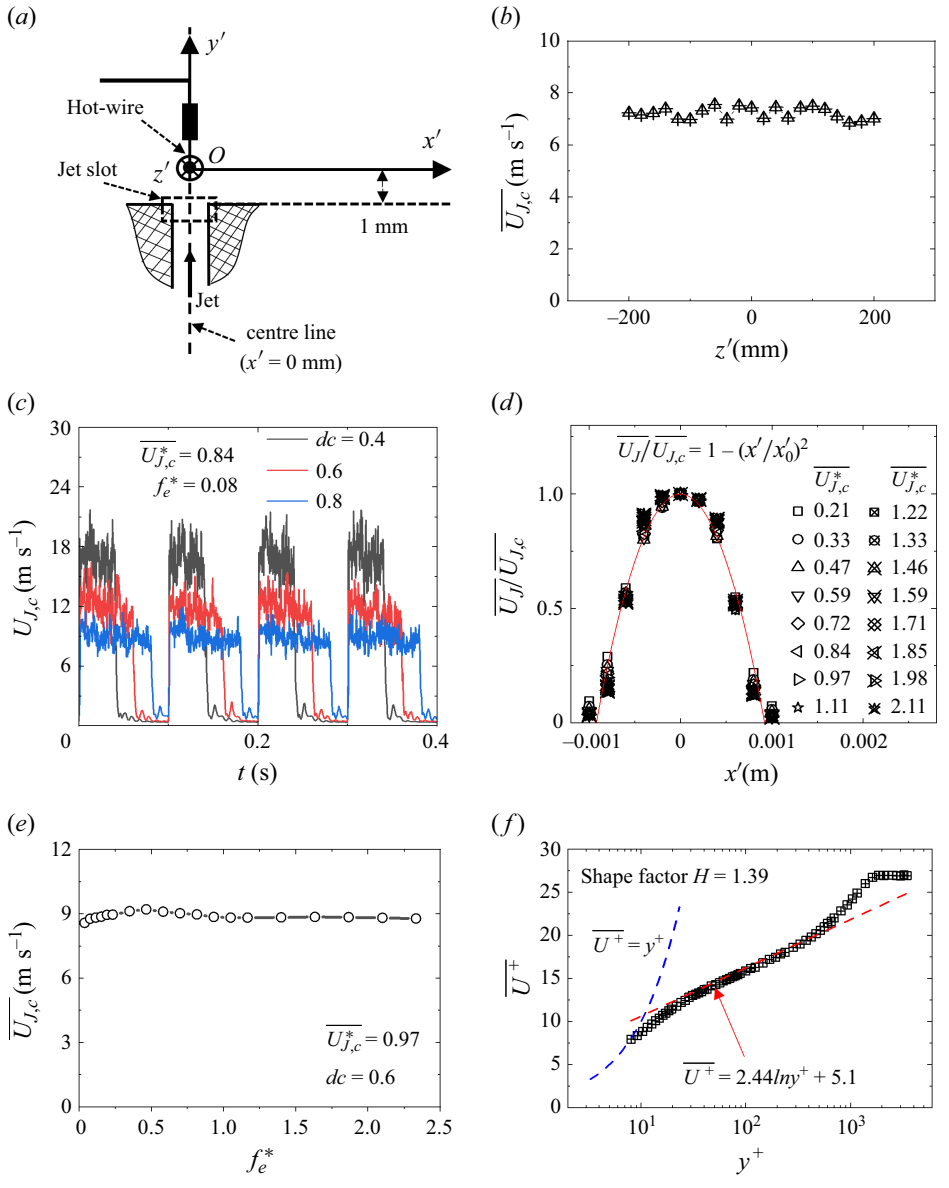



Figure 2. (*a*) Schematic of jet velocity measurement at 1 mm from the exit of control slot jet ($y' = 1$ mm); (*b*) spanwise distribution of $\overline{U_{J,c}}$; (*c*) time histories of the jet velocity $U_{J,c}$; (*d*) $\overline{U_J}/\overline{U_{J,c}}$ along $x'$ ($\pm x'_0$ is the position where $\overline{U_J} = 0$); (*e*) dependence of $\overline{U_{J,c}}$ on $f_e^*$; (*f*) wall-normal distribution of streamwise mean velocity $\overline{U^+}$ normalised by the inner scale at the reference point $P_{ref}$ ($x^* = -5$).

beneficial to the performance of the jet (Haffner *et al.* 2020; Cheng *et al.* 2021). The present length from a solenoid valve to the actuator chamber is reduced to 10 mm, and the actuator chamber is carefully designed to warrant the jet spanwise uniformity and, additionally, a minimal chamber size (figure 1*b*). As shown in figure 2(*e*), the hot-wire-measured $\overline{U_{J,c}}$ is essentially unchanged with $f_e^*$ for a fixed mass flow rate. That is, $\overline{U_{J,c}}$ and $f_e^*$ are decoupled and can be controlled independently.



https://doi.org/10.1017/jfm.2025.10797 Published online by Cambridge University Press

| $U_\infty$ (m s$^{-1}$) | $\delta$ (mm) | $\theta$ (mm) | $\delta_{98}$ (mm) | $H_{12}$ | $u_\tau$ (m s$^{-1}$) | $Re_\theta$ | $Re_h$ |
|---|---|---|---|---|---|---|---|
| 9 | 13.3 | 9.5 | 70 | 1.4 | 0.341 | 5700 | 42 500 |

Table 1. Characteristic parameters of the TBL measured at $x^* = -5$.

It is worth mentioning that the entire system producing the pulsed jet, including the shape and size of the actuator chamber, is identical for different jet angles, except $\alpha$. So are the jet exit characteristics presented in figure 2(*b–e*) when $\alpha$ changes.

The incoming boundary layer velocity profile is measured at a reference point $P_{ref}$, i.e. the endpoint ($x^* = -5$) of the zero-pressure gradient following Song *et al.* (2004) and He *et al.* (2023). It has been confirmed that the measured $\overline{C_p}$ retains zero from $x^* = -15$ to $-5$ on the plate surface (not shown). Table 1 presents the characteristic parameters of the TBL, including the momentum thickness $\theta$, displacement thickness $\delta$, boundary-layer thickness $\delta_{98}$, shape factor $H$, friction velocity $u_\tau$, and $\theta$- and $h$-based Reynolds numbers $Re_\theta$ and $Re_h$. The $u_\tau$ is estimated to be 0.341 m s$^{-1}$ based on fitting the logarithmic profile using the Clauser method (Wei, Schmidt & McMurtry 2005). Here, $Re_\theta$ is 5700, corresponding to $Re_h = 42\,500$. As shown in figure 2(*f*), the logarithmic part of the $\overline{U^+}$ profile collapses well with the classical log law region of the fully developed TBL, *viz.*

$$\overline{U^+} = \frac{1}{\kappa}\ln y^+ + B, \tag{3.2}$$

where $\kappa = 0.41$, $B = 5.1$ and the superscript '+' denotes normalisation by $u_\tau$. The corresponding shape factor ($H$) is approximately 1.4, which is the typical value of a fully developed TBL.

## 4. Parametric study and control mechanisms

### 4.1. *Parametric study for $\alpha \leq 55°$*

The $\overline{C_p}$ distributions (figure 3) are first analysed for different $\overline{U^*_{J,c}}$ and $\alpha$ with fixed $dc$ and $f^*_e$. The $\overline{C_{p,e}}$ marked in figures 3(*a*) and 3(*f*) is the $\overline{C_p}$ value at the end of the ramp. Several observations can be made. First, all the profiles intersect approximately at the same $x^*$, as indicated by the black broken line (figure 3*a–f*). We then divide the flow into regions 1 and 2, i.e. upstream and downstream of the intersection point, respectively. Second, $\overline{C_p}$ displays opposite variations in the two regions, e.g. dropping in region 1 but rising in region 2 (figure 3*a–c*), with increasing $\overline{U^*_{J,c}}$. As such, we may examine how $\overline{C_p}$ varies only in region 2. Third, given $\overline{U^*_{J,c}}$, the smaller $\alpha$, the larger $\overline{C_p}$ in region 2, i.e. $\overline{C_p}(\alpha = 0°) > \overline{C_p}(\alpha = 25°) > \overline{C_p}(\alpha = 55°) > \overline{C_p}(\alpha = 70°) > \overline{C_p}(\alpha = 85°) > \overline{C_p}(\alpha = 115°)$. Fourth, a large $\overline{C_p}$ or pressure recovery is achieved with increasing $\overline{U^*_{J,c}}$ for $\alpha \leq 55°$ (figure 3*a–c*), which is beneficial to our control target; however, this is opposite for $\alpha > 55°$, that is, $\overline{C_p}$ drops with increasing $\overline{U^*_{J,c}}$ (figure 3*d–f*). Apparently, the underlying flow physics under jet control must have changed from one $\alpha$ range to the other. Therefore, we will separately analyse and discuss the results of the two $\alpha$ ranges in § 4.1–4.2 and § 4.3–4.4, respectively.

The control target is to reduce the flow separation region and consequently to recover the pressure loss caused by flow separation. Since over one thousand sets of control parameters are presently examined, it would be infeasible to conduct PIV measurements for each case to determine accurately the separation bubble size $\overline{L^*}$. It is thus important to find a landmark pressure as the indicator for variation in $\overline{L^*}$ and hence the pressure recovery.



https://doi.org/10.1017/jfm.2025.10797 Published online by Cambridge University Press

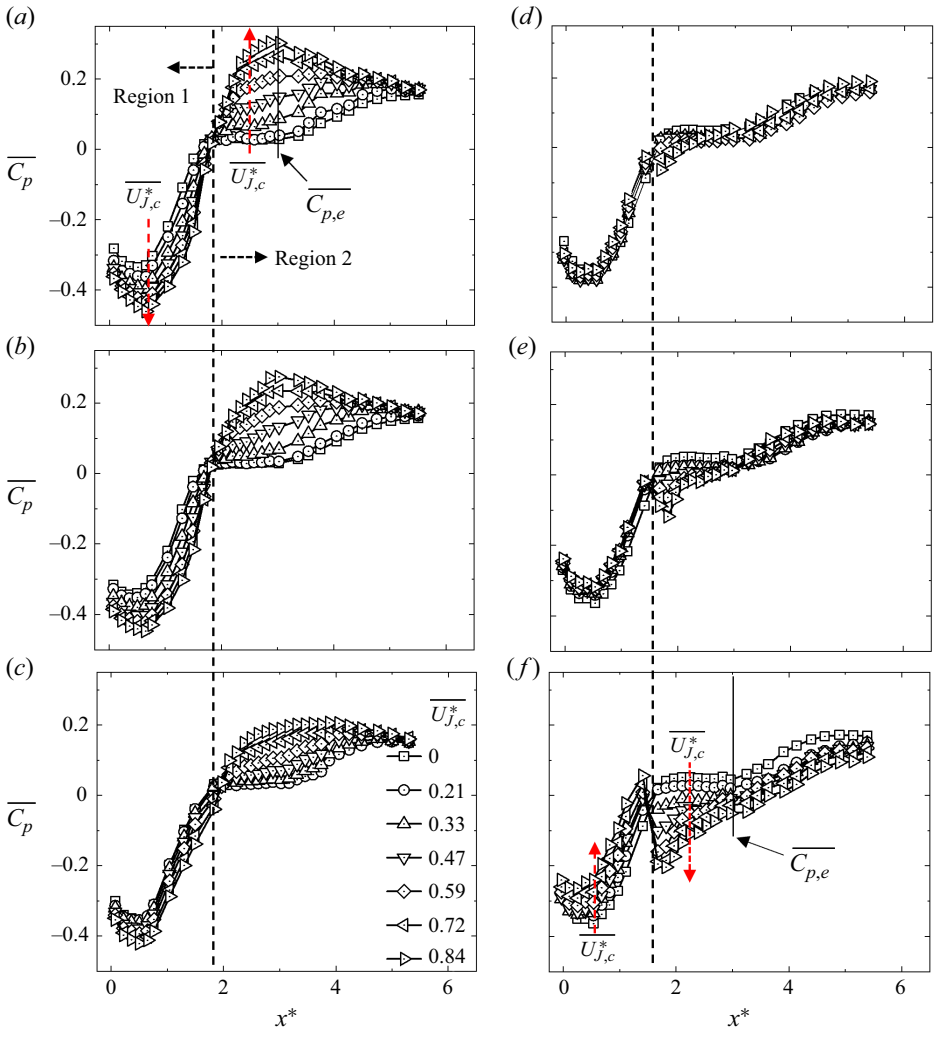



Figure 3. Longitudinal distribution of time-averaged pressure coefficient $\overline{C_p}$ on the ramp at different $\overline{U^*_{J,c}}$ ($dc = 0.4$, $f^*_e = 0.23$): (*a*) jet blowing angle $\alpha = 0°$; (*b*) 25°; (*c*) 55°; (*d*) 70°; (*e*) 85°; (*f*) 115°. The vertical black broken line marks the position of the intersection point of the $\overline{C_p}$ profiles, the red broken-lined arrows indicate how $\overline{C_p}$ would vary with increasing $\overline{U^*_{J,c}}$, and the black solid line denotes the position of $\overline{C_{p,e}}$.

In the experimental study of controlling flow separation from a backward-facing ramp, Hlevca, Gilliéron & Grasso (2018) used $\overline{C_p}$ at the end of the ramp, i.e. $\overline{C_{p,e}}$, to evaluate the control performance. He *et al.* (2023) qualitatively observed a negative correlation between $\overline{L^*}$ and $\overline{C_{p,e}}$. In fact, the present data show that $\overline{L^*}$ and $\overline{C_{p,e}}$ are negatively correlated for $\alpha \leq 55°$ (figure 4*a*). As marked by the red star in figure 4(*a*), the recirculation region completely disappears at $\overline{C_{p,e}} \approx 0.2$. As $\overline{C_{p,e}}$ increases, $\overline{x^*_s}$ shifts downstream and, meanwhile, the reattachment point $\overline{x^*_r}$ moves upstream (figure 4*b*), resulting in a reduced $\overline{L^*}$ ($\overline{L^*} = \overline{x^*_r} - \overline{x^*_s}$). Evidently, the variation in $\overline{C_{p,e}}$, denoted by $\Delta\overline{C_{p,e}}$, is an excellent indicator for the evaluation of control performance, *viz.*

$$\Delta\overline{C_{p,e}} = \overline{C_{p,e}} - \overline{C_{p,e0}}, \tag{4.1}$$



https://doi.org/10.1017/jfm.2025.10797 Published online by Cambridge University Press

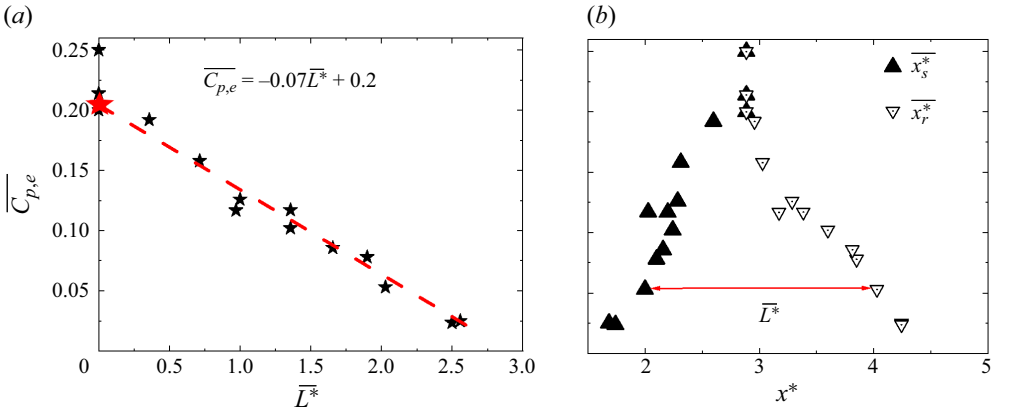



Figure 4. Dependence of $\overline{C_{p,e}}$ on (*a*) the separation bubble length $\overline{L^*}$ ($\alpha \leq 55°$), where the red star is the $\overline{C_{p,e}}$ value corresponding to $\overline{L^*} = 0$ and the red dashed line is the least-squares fitting to the measured data, and (*b*) the time-averaged separation and reattachment points, $\overline{x_s^*}$ and $\overline{x_r^*}$.

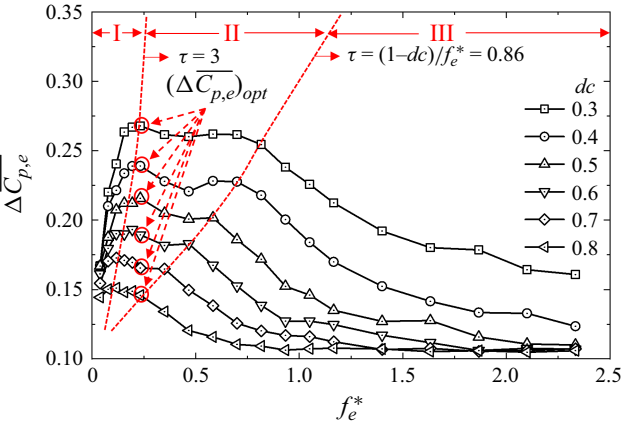



Figure 5. Dependence of $\Delta\overline{C_{p,e}}$ on the excitation frequency $f_e^*$ ($\overline{U_{J,c}^*} = 0.72$, $\alpha = 0°$).

where $\overline{C_{p,e}}$ and $\overline{C_{p,e0}}$ are the time-averaged pressure coefficient with and without control, respectively, at the end of ramp.

A parametric study is carried out to investigate the dependence of $\Delta\overline{C_{p,e}}$ on $\overline{U_{J,c}^*}$, d*c*, $f_e^*$ and $\alpha$. The relationship between $\Delta\overline{C_{p,e}}$ and $f_e^*$ is complicated (figure 5), and can be divided into three regions, i.e. I, II and III. In region I, $\Delta\overline{C_{p,e}}$ rises rapidly with increasing $f_e^*$ and the rising rate depends on *dc*. A smaller *dc* yields a more rapid rise. In region II, $\Delta\overline{C_{p,e}}$ changes little with increasing $f_e^*$. In region III, $\Delta\overline{C_{p,e}}$ drops slowly with increasing $f_e^*$ and eventually levels off. It is worth noting that the critical $f_e^*$ at which region II changes to III varies with *dc*. For instance, as marked by the red dashed line, the critical $f_e^*$ is approximately 0.82 for $dc = 0.3$, but drops to 0.23 for $dc = 0.8$. However, $\tau$ remains constant, 0.86 at the point that separates regions II and III, and approximately 3 at the point that separates regions I and II, where

$$\tau = \frac{1 - dc}{f_e^*} \tag{4.2}$$



https://doi.org/10.1017/jfm.2025.10797 Published online by Cambridge University Press

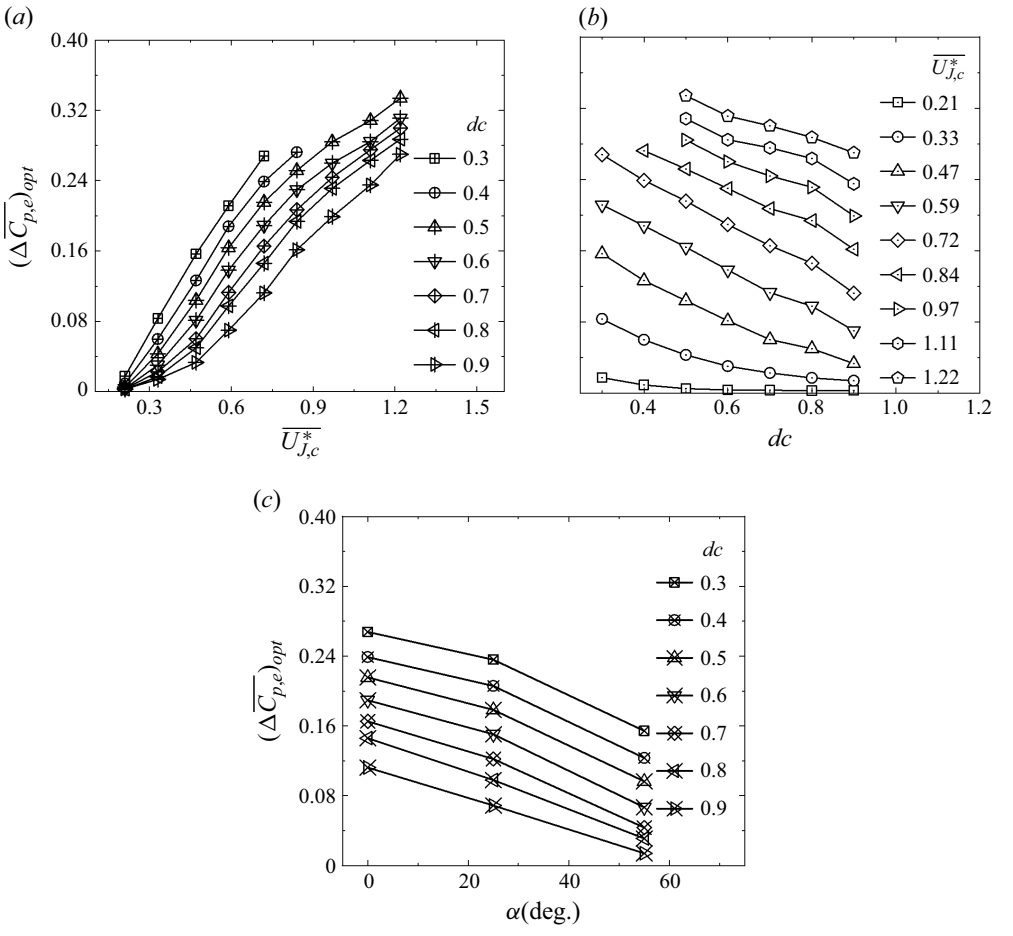



Figure 6. Dependence of $(\Delta\overline{C_{p,e}})_{opt}$ on (*a*) $\overline{U^*_{J,c}}$ for various $dc$ ($\alpha = 0°$, $f_e^* = 0.23$), (*b*) $dc$ for various $\overline{U^*_{J,c}}$ ($\alpha = 0°$, $f_e^* = 0.23$) and (*c*) $\alpha$ for various $dc$ ($\overline{U^*_{J,c}} = 0.72$, $f_e^* = 0.23$).

represents the dimensionless duration during which the jet is closed in one period of the pulsed jet. Note that $(\Delta\overline{C_{p,e}})_{opt}$ in figure 5 is the $\Delta\overline{C_{p,e}}$ value at $f_e^* = 0.23$, at which the maximum $\Delta\overline{C_{p,e}}$ takes place for a given $\overline{U^*_{J,c}}$ and $dc$.

As shown in figure 6(*a*), $(\Delta\overline{C_{p,e}})_{opt}$ rises monotonously with increasing $\overline{U^*_{J,c}}$, regardless of $dc$, given $f_e^*$ and $\alpha$ since a large $\overline{U^*_{J,c}}$ enhances the Coanda effect, thus suppressing flow separation and promoting pressure recovery (He *et al.* 2023). Note that, limited by the solenoid valve used to produce the pulsed jet, there is a lack of data at very large $\overline{U^*_{J,c}}$ and small $dc$, e.g. at $dc = 0.3$ and 0.4 for $\overline{U^*_{J,c}} \geq 0.84$. The relationship between $(\Delta\overline{C_{p,e}})_{opt}$ and $\overline{U^*_{J,c}}$ is nonlinear, though qualitatively unchanged despite a variation in $dc$. However, given $f_e^*$ and $\alpha$, $(\Delta\overline{C_{p,e}})_{opt}$ drops monotonously and nonlinearly from $dc = 0.3$–$0.9$, irrespective of $\overline{U^*_{J,c}}$ (figure 6*b*). For a fixed $\overline{U^*_{J,c}}$ or mass flow rate, a smaller $dc$ will produce a larger maximum jet velocity (figure 2*c*), thus enhancing the Coanda effect and causing a rise in $(\Delta\overline{C_{p,e}})_{opt}$. Additionally, $(\Delta\overline{C_{p,e}})_{opt}$ exhibits a strong dependence on $\alpha$ (figure 6*c*), dropping monotonously with increasing $\alpha$ for all $dc$. This is reasonable as a small $\alpha$ implies



https://doi.org/10.1017/jfm.2025.10797 Published online by Cambridge University Press

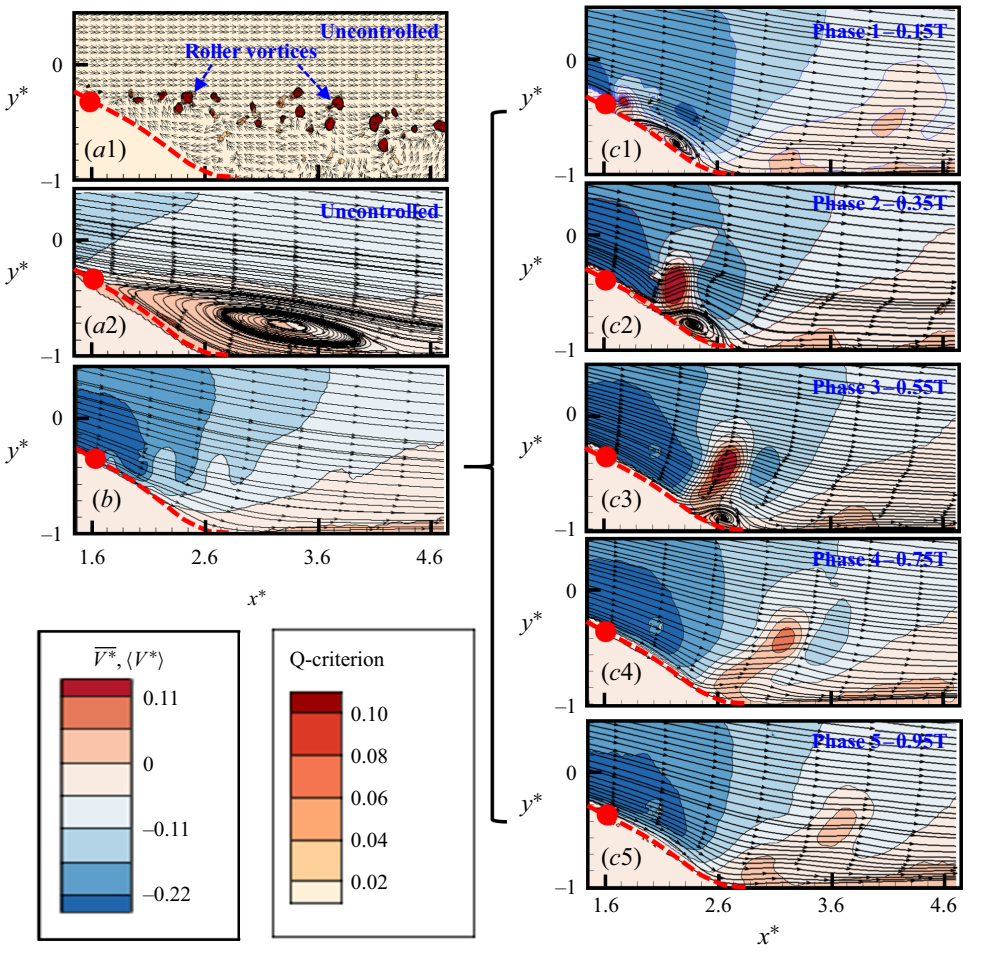



Figure 7. PIV data with and without forcing: (*a1*) unforced instantaneous iso-contours of Q-Criterion superimposed with velocity vectors; (*a2*) unforced time-averaged streamlines superimposed with the velocity component $\overline{V^*}$; (*b*) time-averaged streamlines superimposed with $\overline{V^*}$ (forced at $\alpha = 0°$, $\overline{U^*_{J,c}} = 0.59$, $dc = 0.3$, $f^*_e = 0.25$) when $\overline{C_{p,e}} (\approx 0.2)$ corresponds to the red star in figure 4(*a*); (*c1–c5*) phase-averaged streamlines superimposed with $\langle V^* \rangle$. $T$ is the period of the control jet, the red dashed curves represent the ramp and the red dot denotes the control jet position.

a larger tangential component of the jet and thus a stronger Coanda effect. The optimal control performance is achieved at $\alpha = 0°$.

### 4.2. *Control mechanism for $\alpha \leq 55°$*

To gain an understanding of the flow physics and control mechanism, we analyse the PIV-measured velocity data in the $x$–$y$ plane. In the baseline flow, a series of roller vortices originating from the Kelvin–Helmholtz instability are identified by Q-Criterion in figure 7(*a1*), and a recirculation region or separation bubble below these vortices is evident. The flapping of the vortices forms the high Reynold stresses and turbulent kinetic energy above the separation bubble. Inside the separation bubble, Reynold stresses and turbulent kinetic energy is relatively small (Song *et al.* 2004; He *et al.* 2023). Under control ($\alpha = 0°$, $\overline{U^*_{J,c}} = 0.59$, $dc = 0.3$ and $f^*_e = 0.25$), the recirculation region, as



https://doi.org/10.1017/jfm.2025.10797 Published online by Cambridge University Press

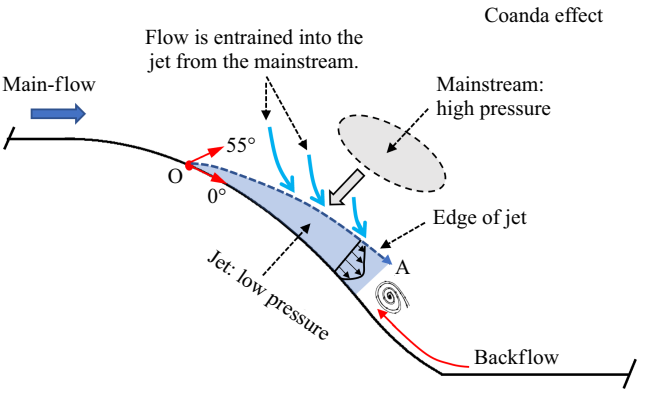



Figure 8. Schematic of the flow physics under control when the jet angle $\alpha = 0°$–$55°$. Point O denotes the jet position. A small vortex A results from the interaction between the pulsed jet and the backflow. Blue arrows indicate the flow entrained from the mainstream into the jet.

shown in figure 7(*a*2) in the absence of control, vanishes completely, accompanied by a massive downward motion, as indicated by almost entirely negative $\overline{V^*}$ above the ramp (figure 7*b*). The roller vortices also disappear due to the suppressed flow separation. The phase-averaged streamlines superimposed with $\langle V^* \rangle$ (figure 7*c1–c5*) indicate that each jet injection generates one clockwise-rotating spanwise vortex downstream (figure 7*c1*). This vortex grows when advected downstream (figure 7*c1–c2*), though vanishing upon reaching the downstream plate surface (figure 7*c3–c5*). A massive downward motion is generated upstream of this spanwise vortex, resulting in the flow attached to the wall.

A schematic is proposed in figure 8 on the physical mechanism of the suppressed flow separation from the ramp. The jet induces the Coanda effect, producing a low-pressure region between the jet and the wall with respect to the mainstream (Warsop *et al.* 2018; Xu *et al.* 2022). The pressure difference between the mainstream and the near-wall region not only offsets the centrifugal force of the blowing jet (Englar 2000), but also produces a massive downward fluid motion towards the curved ramp (figures 7*b* and 7*c1–c5*), forcing the separated flow attached to the wall. As a result, the recirculation region contracts and the pressure on the wall recovers. As the jet entrains fluid from only the upper side, i.e. the mainstream, unlike a free jet entraining fluid from both sides, the entrainment rate is higher than a free jet (Warsop *et al.* 2018; Xu *et al.* 2018). Thus, the jet grows in width and its mean velocity decreases downstream at a higher rate than a free jet, which is associated with a pressure rise in the jet. When the pressure difference between the jet and the mainstream vanishes, the flow may separate again. Note that a small spanwise vortex A occurs downstream of the blowing jet, resulting from the interaction between the pulsed jet and the backflow near the wall due to flow recirculation. This vortex A is absent under steady jet control (He *et al.* 2023).

### 4.3. *Parametric study for $\alpha > 55°$*

In this section, we examine closely the data of $\alpha > 55°$, where the $\overline{C_p}$ distributions display a difference in variation with $\overline{U^*_{J,c}}$ from those of $\alpha \leq 55°$ (figure 3), suggesting different flow physics involved under control.

Let us first examine the pre-multiplied energy spectra of $u$ measured in the absence of control. The measurement points A–K with 5 mm intervals along the $y$-direction are chosen at the end of the ramp (figure 9*a*). Figure 9(*b*) is the dependence of $\overline{u^2}$ on $y$. As noted in the investigation on flow separation from a curved ramp by Song & Eaton



https://doi.org/10.1017/jfm.2025.10797 Published online by Cambridge University Press

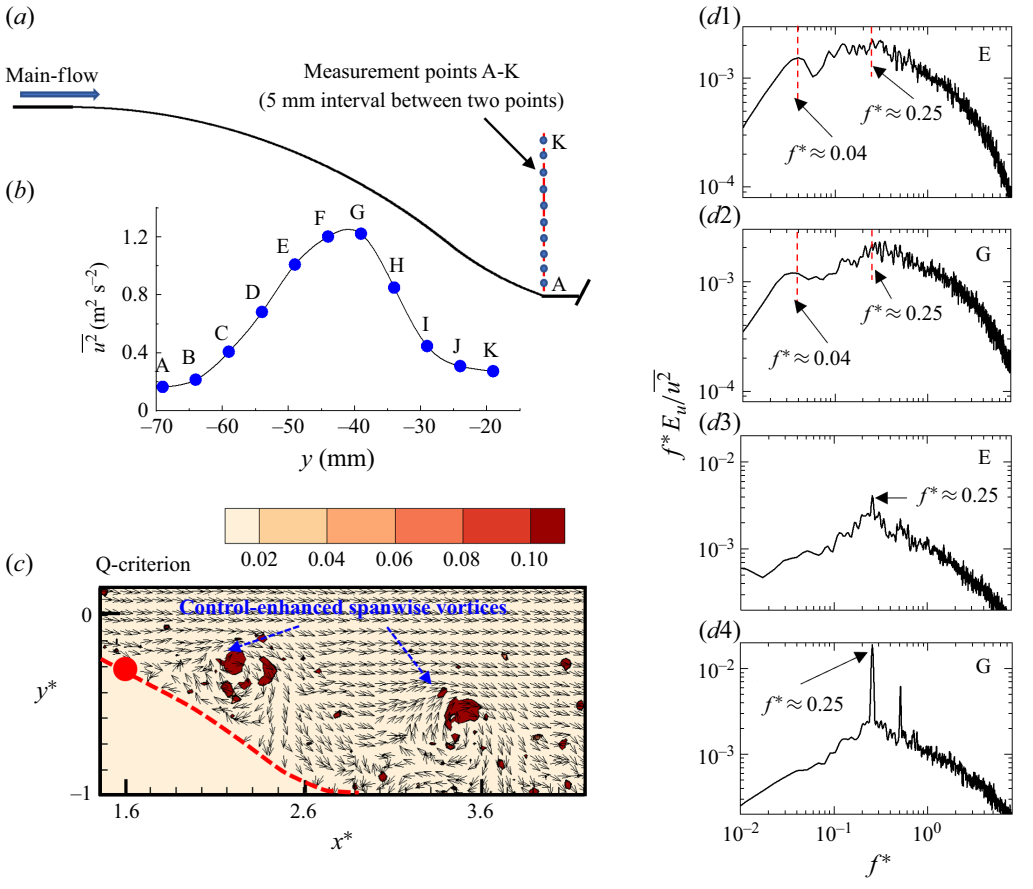



Figure 9. (*a*) Schematic of the measurement positions; (*b*) dependence of $\overline{u^2}$ on the measurement position in the absence of control; (*c*) instantaneous iso-contours of Q-Criterion superimposed with velocity vectors under control; (*d*) pre-multiplied energy spectra of $u$ measured at positions E and G in the baseline flow (*d*1–*d*2) and under control (*d*3–*d*4: $\alpha = 115°$, $\overline{U^*_{J,c}} = 0.59$, $dc = 0.3$, $f^*_e = 0.25$).

(2004), the turbulence is inactive within the separation bubble, while the high turbulent kinetic energy region is caused by the flapping motion of roller vortices, resulting from the Kelvin–Helmholtz instability in the separated shear layer. The roller vortices are evident from the Q-Criterion (figure 7*a*1). The pre-multiplied energy spectra (figure 9*d*1–*d*2) of the baseline flow at positions E and G (figure 9*b*), where $\overline{u^2}$ is large, display two appreciable peaks at $f^* \approx 0.04$ and 0.25. The peak at $f^* \approx 0.04$ is associated with the flapping motion or shear layer flapping, which is quite close to that observed by Chiatto, Luca & Grasso (2021) in a 3-D flow around a backward facing ramp, with a 25° slope angle. However, the peak at $f^* \approx 0.25$ is due to the natural vortex shedding or roller vortices (figure 7*a*1)**.** Under control, the spectra (figure 9*d*3–*d*4) display several differences. The spectral peak associated with flapping motion disappears completely. At $f^*_e = 0.25$, the spectrum shows a predominant and sharp peak at the excitation frequency, the other peak at higher frequency being its harmonic. This sharp peak is ascribed to the large-scale spanwise vortices generated by the control jet (figure 9*c*). Apparently, the control suppresses the flapping motion on one hand and strengthens greatly vortex shedding on the other hand.



https://doi.org/10.1017/jfm.2025.10797 Published online by Cambridge University Press

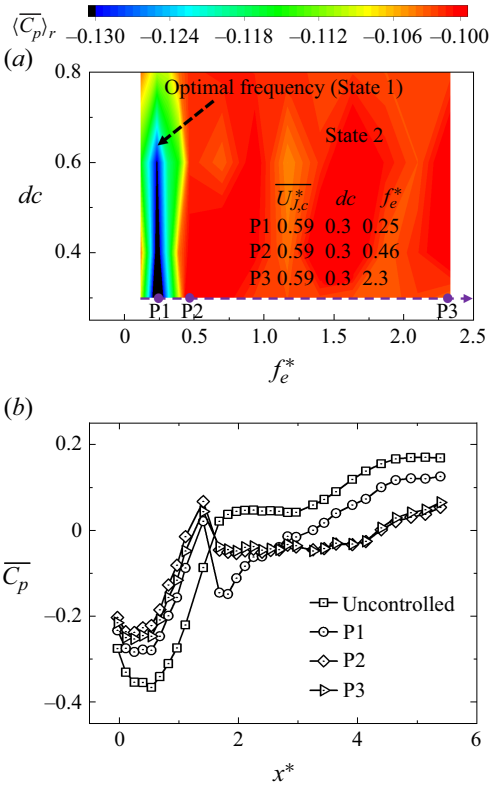



Figure 10. (*a*) Dependence on $f_e^*$ and $dc$ of space- and time-averaged pressure coefficient $\langle\overline{C_p}\rangle_r$ on the ramp ($\alpha = 115°$, $\overline{U^*_{J,c}} = 0.59$); (*b*) longitudinal distributions of $\overline{C_p}$ for selected cases in (*a*) and baseline flow, where State 1 corresponds to the control under the optimal frequency and State 2 denotes the cases when control performance is independent of $dc$ and $f_e^*$.

Unlike the case of $\alpha \leq 55°$ where a specific $\overline{C_{p,e}}$ or $\Delta\overline{C_{p,e}}$ corresponds to only one $\overline{C_p}$ distribution and hence one separation bubble size, one $\overline{C_{p,e}}$ may correspond to different $\overline{C_p}$ distributions for $\alpha > 55°$. One example is given in figure 10(*b*), where cases P1, P2 and P3 correspond to jet control at $f_e^* = 0.25$ (synchronising with the natural vortex shedding frequency), 0.46 and 2.3, respectively (other control parameters are given in figure 10*a*). Furthermore, the relationship between $\overline{C_{p,e}}$ and $\overline{L}^*$ in figure 4 does not hold anymore. As such, it would be inappropriate to use $\Delta\overline{C_{p,e}}$ as a valid indicator for control performance. Following Zhang *et al.* (2018) and Haffner *et al.* (2020), we use the space- and time-averaged pressure coefficient $\langle\overline{C_p}\rangle_r$ as the indicator for control performance, which is defined by

$$\langle\overline{C_p}\rangle_r = \frac{1}{n}\sum_{k=1}^{n}\overline{C_{p,k}}, \tag{4.3}$$

where $n = 20$ is the number of pressure taps on the ramp.

We examine $\langle\overline{C_p}\rangle_r$ only at $\alpha = 115°$ since the results are qualitatively similar for $\alpha = 115°$, 85° and 70°. The $\langle\overline{C_p}\rangle_r$ displays a dependence on $f_e^*$ and $dc$, especially about the optimal excitation frequency $f_e^* = 0.25$. Away from 0.25, $\langle\overline{C_p}\rangle_r$ varies little with $dc$



https://doi.org/10.1017/jfm.2025.10797 Published online by Cambridge University Press

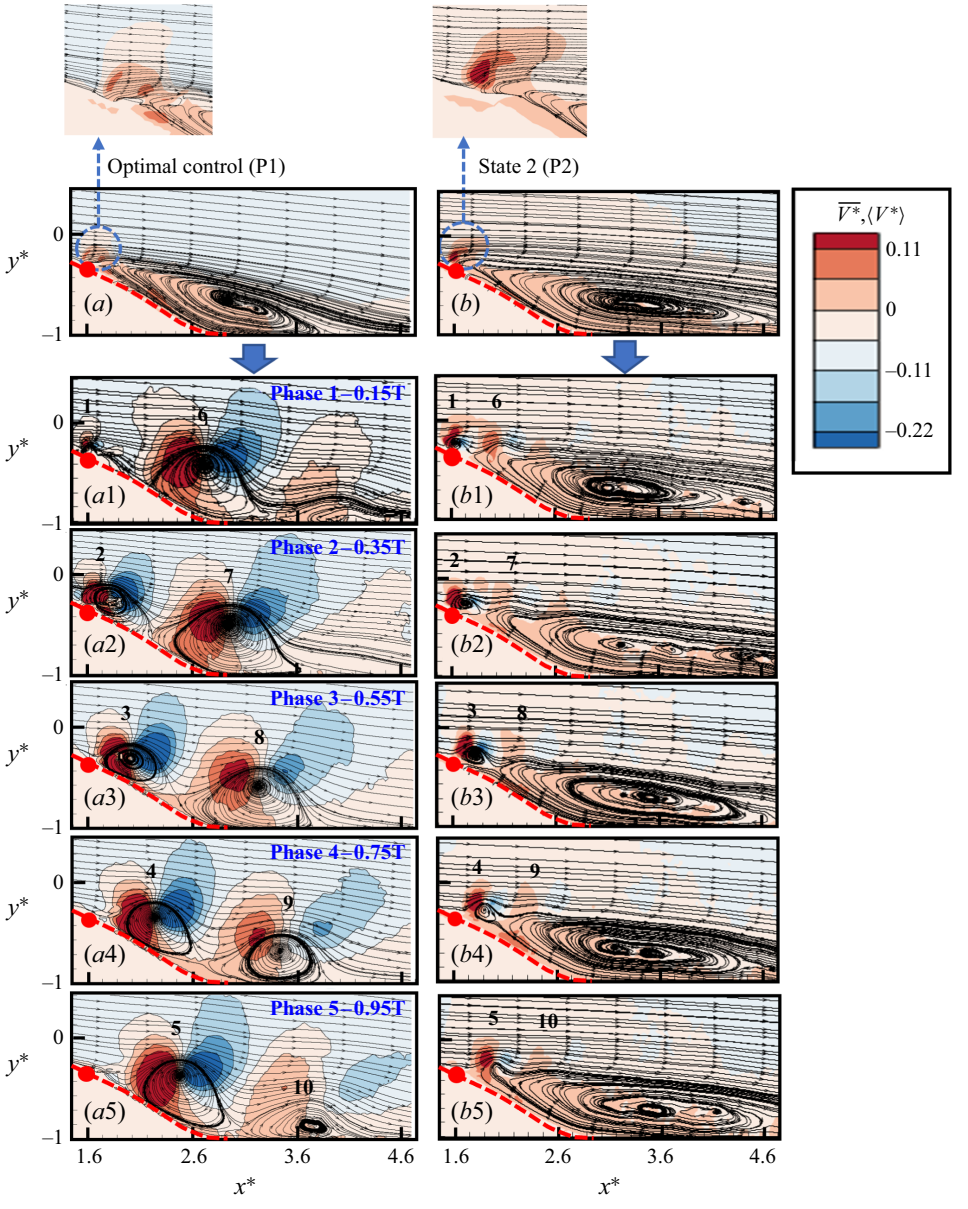



Figure 11. PIV time-averaged streamlines and iso-contours of $\overline{V^*}$ of (*a*) case P1 and (*b*) case P2; phase-averaged streamlines superimposed with $\langle V^* \rangle$ of (*a*1–*a*5) case P1 and (*b*1–*b*5) case P2. Red dashed curve represents the ramp and the red dot denotes the jet position.

and $f_e^*$, and depends on only $\overline{U_{J,c}^*}$ and $\alpha$. Under control, $\overline{C_p}$ rises, compared with the uncontrolled case, and reaches its maximum at $x^* \approx 1.65$ where the control jet issues and then drops, especially at $f_e^* = 0.25$ (case P1). The longitudinal $\overline{C_p}$ distribution at $f_e^* = 0.25$ shows an appreciable difference from those, such as cases P2 and P3, away from 0.25. However, the $\overline{C_p}$ distributions corresponding to cases P2 and P3 collapse quite well. It is noteworthy that there is no similar optimal value of excitation frequency identified when $\alpha \leq 55°$.



https://doi.org/10.1017/jfm.2025.10797 Published online by Cambridge University Press

### 4.4. *Control mechanism for $\alpha > 55°$*

To clear the flow physics for $\alpha > 55°$, the flow fields of cases P1 and P2 are presented in figure 11. Figures 11(*a*) and 11(*b*) show time-averaged streamlines superimposed with iso-contours of $\overline{V^*}$ for cases P1 and P2, respectively, and figures 11(*a1–a5*) and 11(*b1–b5*) present the corresponding phase-averaged streamlines superimposed with $\langle V^* \rangle$. The two vortices in each plate of the phase-averaged data, such as vortices 1 and 6 in figure 11(*a1*), are generated by two consecutive jet pulses, because they have a time interval of $1.2T$. In the adjacent plates, the corresponding two vortices, such as vortex 1 in figure 11(*a1*) and vortex 2 in figure 11(*a2*), have a time interval of $0.2T$. This suggests that they are from the same jet pulse, occurring at different moments. After the spanwise vortex is generated at the jet exit, its lifecycle or motion follows the sequence of $1 \rightarrow 2 \rightarrow 3 \rightarrow 4 \rightarrow 5 \rightarrow 6 \rightarrow 7 \rightarrow 8 \rightarrow 9 \rightarrow 10$ (figure 11*a1–a5*). As the vortex moves downstream, its core intensity keeps impairing; its size grows from 1 to 6 and then contracts from 7 to 10 before eventual vanishment downstream. Each pulse of the slit jet generates a large spanwise vortex (figure 11), as produced by the synthetic jet issued from a slit (Dandois *et al.* 2007), which is different from a hairpin vortex or distorted vortex-ring produced by circular synthetic jets (Palumbo *et al.* 2022). When the pulsed-jet frequency is close to the natural vortex shedding frequency (case P1), the spanwise vortex is significantly intensified, as shown in figure 11(*a1–a5*) (cf. figure 11*b1–b5*). Upwash flow is formed on the left side of the vortex core, while downwash flow is generated on the right side (figure 11*a1–a5*). This leads to strong momentum transfer, hence resulting in a slight reduction in the recirculation region (figure 11*a*). Zhang & Zhong (2011) also observed in the control of flow separation from a curved ramp that the jet-generated hairpin vortices are significantly intensified when the actuation frequency of the round-hole synthetic jet is close to the natural shedding frequency. In the study on flow separation control over a wall-mounted hump, Greenblatt *et al.* (2006) found that when the spanwise slot synthetic jets are operated near the shear layer frequency, the spanwise vortices produced by the jets may merge with the shedding vortices to form larger-scale spanwise vortical structures, which postpones flow separation. For actuation frequency away from the natural shedding frequency, such as case P2, the jet also generates spanwise vortices. Unlike those in case P1, the vortices in case P2 are significantly weaker and dissipate rapidly when moving downstream (figure 11*b1–b5*), failing to create as strong a momentum exchange as in case P1 (figure 11*a1–a5*). However, as shown by He *et al.* (2023), the upward jet injects momentum into the incoming shear layer and behaves as a tiny spoiler. Please refer to the zoom-in part of figure 11(*a–b*). This effect results in the separating shear layer deviating away from the wall. Consequently, the corresponding reattachment points shift substantially downstream and the separation bubble enlarges in case P2.

Combining cases P1 and P2 of pulsed jet control as well as steady jet control (He *et al.* 2023) for $\alpha > 55°$, a conceptual schematic is summarised in figure 12. The pulsed control jet produces two effects. First, the upward jet injects momentum into the incident shear layer and acts to enlarge the separation bubble (control effect 1). Second, the jet generates a clockwise spanwise vortex, acting to enhance momentum transfer and to reduce the separation bubble size (control effect 2). For steady jet control, there is only the former effect and thus the separation bubble grows (figure 12*c*). In case P1 of the pulsed jet control, the spanwise vortices are markedly strengthened when the excitation frequency is close to the natural vortex shedding frequency. As such, the latter effect dominates and the separation bubble contracts slightly (figure 12*a*). In case P2, the former effect dominates since the spanwise vortices are relatively weak, thus causing the separation bubble to grow (figure 12*b*).



https://doi.org/10.1017/jfm.2025.10797 Published online by Cambridge University Press

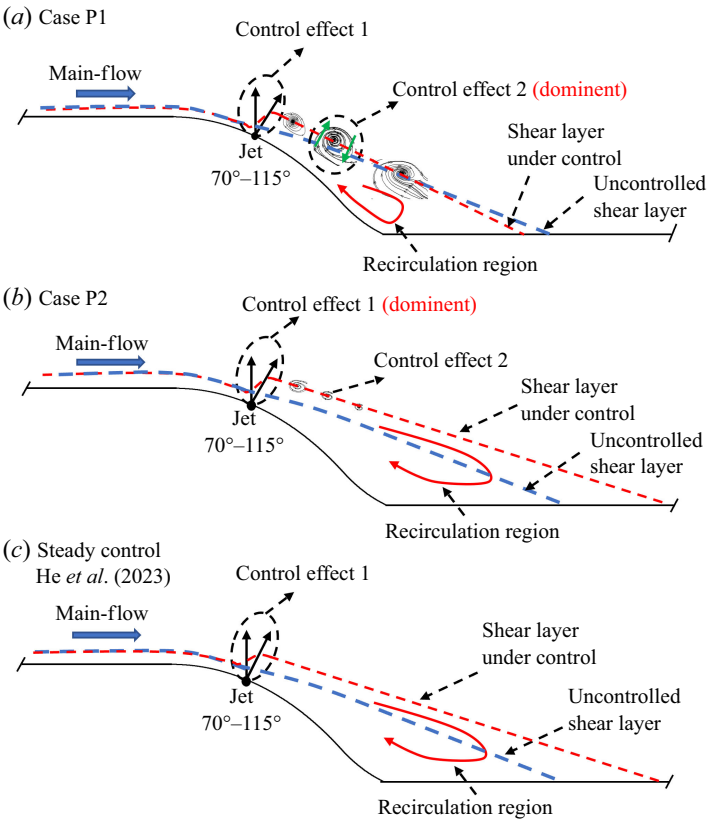



Figure 12. Schematic of flow physics under control when the jet angle $\alpha > 55°$: (*a–b*) pulsed jet; (*c*) steady jet. The green arrows denote the upwash and downwash flows generated by spanwise vortices. The red solid curves with an arrow indicate the recirculation region under control. The red and blue dashed lines represent the shear layers with and without control, respectively. The black solid arrows represent the jet directions.

## 5. Scaling analysis

### 5.1. *Analysis of* $\overline{U^*_{J,c}}$ *and* $dc$

An empirical scaling analysis is performed for $\alpha \leq 55°$ in this section. Valuable insight into the flow physics and control mechanisms behind the influence of control parameters on flow separation may be gained from this analysis.

The energy ratio $\gamma$ of the control jet to the mainstream per unit area may be given by

$$\gamma = \frac{\left(\int_0^{nT} 0.5\dot{m}_\infty U_{J,c}^2 \mathrm{d}t\right)/nT}{\left(\int_0^{nT} 0.5\dot{m}_{J,c} U_\infty^2 \mathrm{d}t\right)/nT} = \frac{\overline{U_{J,c}^3}}{U_\infty^3} = \overline{U_{J,c}^{*3}}, \tag{5.1}$$

where $n$ represents the cycle number of the pulsed jet ($n \geq 100$), $T$ is the period of the control jet, $\dot{m}_\infty = \rho U_\infty$ and $\dot{m}_{J,c} = \rho U_{J,c}$ are the mass flow rates per unit area of main flow and jet, respectively, and $0.5\dot{m}_{J,c}U_{J,c}^2$ and $0.5\dot{m}_\infty U_\infty^2$ are the instantaneous power per unit area of the jet and main flow, respectively. After careful theoretical and experimental data analyses, it has been found that all the data points of $(\Delta\overline{C_{p,e}})_{opt}$ in figure 6(*a–b*) collapse about a curve, regardless of $\overline{U^*_{J,c}}$ and $dc$, once being presented as the function of $\gamma$ (figure 13*a*) or $\gamma^{1/3}$ (figure 13*b*). The observation suggests that $\gamma$ is the controlling



https://doi.org/10.1017/jfm.2025.10797 Published online by Cambridge University Press

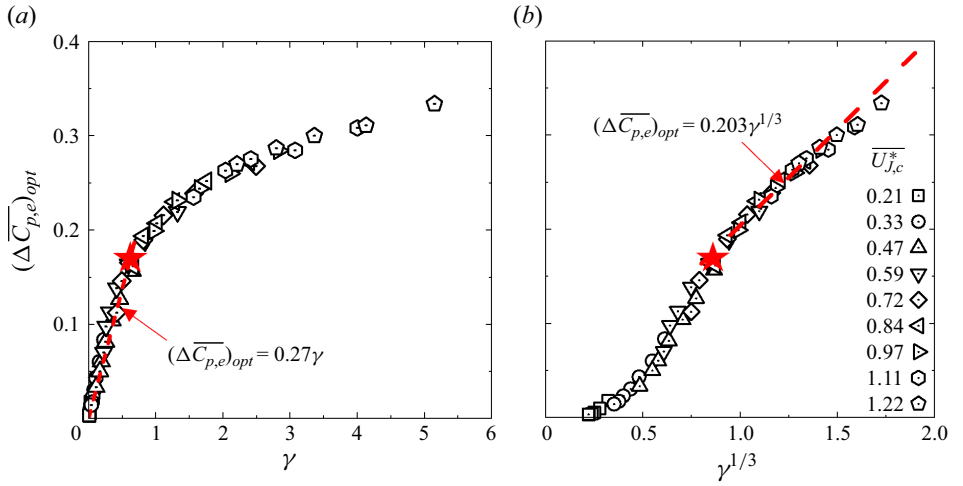



Figure 13. Dependence of $(\Delta\overline{C_{p,e}})_{opt}$ on (*a*) the jet energy ratio $\gamma$ and (*b*) $\gamma^{1/3}$, including all data points in figure 6(*a–b*) ($\alpha = 0°$, $f_e^* = 0.23$, $dc = 0.3, 0.4, \ldots, 0.9$). The red dashed curves in panels (*a*) and (*b*) are least-squares fitting to data points at $\gamma < 0.7$ and $\gamma \geq 0.7$, respectively. The red star, corresponding to the red star in figure 4, represents the critical point where the separation bubble disappears.

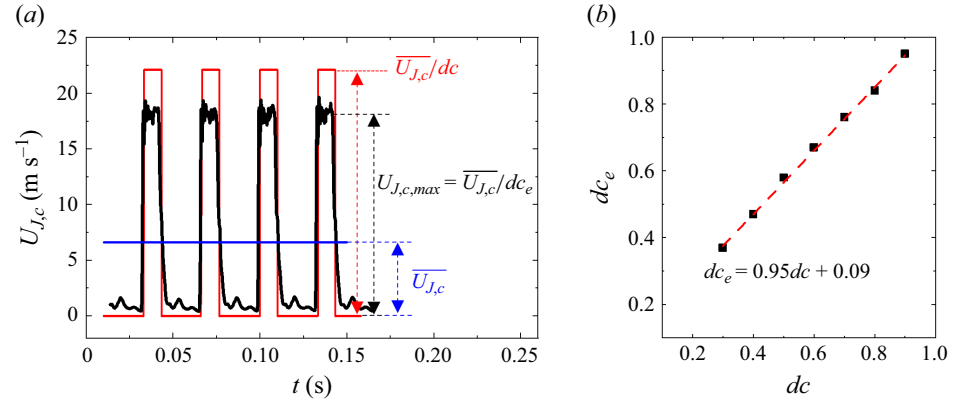



Figure 14. (*a*) Hotwire-measured time history of $U_{J,c}$ ($\overline{U^*_{J,c}} = 0.72$, $dc = 0.3$, $f_e^* = 0.23$), where the red-colored curve is the theoretical time history calculated from $dc$ and $\overline{U_{J,c}}$, as indicated by the horizontal blue line; (*b*) correlation between the effective duty cycle $dc_e$ and $dc$.

scaling factor; that is, $(\Delta\overline{C_{p,e}})_{opt}$ or the separation bubble size is the same for a fixed $\gamma$, irrespective of different mean velocity ratio and duty cycle. Note that a larger mean velocity ratio or smaller duty cycle leads to a larger $\gamma$ and hence a larger $(\Delta\overline{C_{p,e}})_{opt}$. This explains why $(\Delta\overline{C_{p,e}})_{opt}$ rises monotonically with increasing mean velocity ratio and decreasing duty cycle (figure 6*a–b*).

Since energy ratio $\gamma$ is obtained from hot-wire measurement and depends on mean velocity ratio and duty cycle, one question arises. Can $\gamma$ be expressed as a combination of mean velocity ratio and duty cycle? As indicated by the red solid curve in figure 14(*a*), if the time history of the jet velocity is an ideal square wave, (5.1) can be theoretically



https://doi.org/10.1017/jfm.2025.10797 Published online by Cambridge University Press

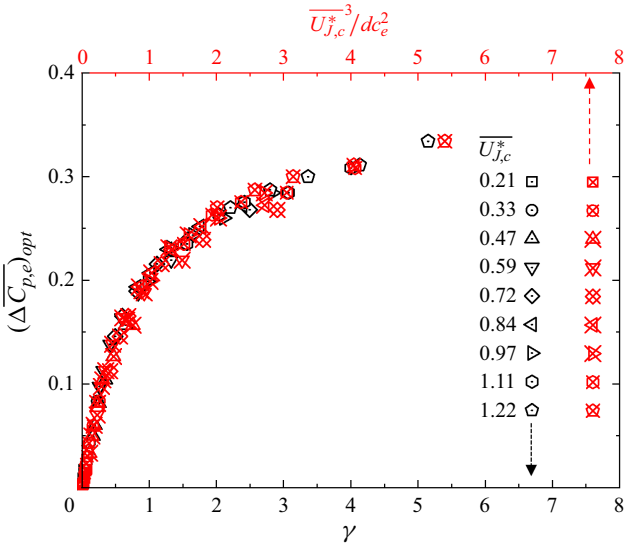



Figure 15. Comparison between the dependences of $(\Delta\overline{C_{p,e}})_{opt}$ on $\gamma$ and $\overline{U^*_{J,c}}^3/dc_e^2$ ($\alpha = 0°$, $f^*_e = 0.23$, $dc = 0.3, 0.4, \ldots, 0.9$).

rewritten as

$$\text{Energy ratio} = \frac{\left(\int_0^{nT} 0.5 m_{J,c} U_{J,c}^2 \mathrm{d}t\right)/nT}{\left(\int_0^{nT} 0.5 m_\infty U_\infty^2 \mathrm{d}t\right)/nT} = \frac{\left(\frac{\overline{U_{J,c}}}{\mathrm{d}c}\right)^3 \mathrm{d}c nT}{U_\infty^3 nT} = \frac{\overline{U^*_{J,c}}^3}{\mathrm{d}c^2}, \tag{5.2}$$

where $\overline{U_{J,c}}/dc$ is the nominal maximum value of the jet velocity. However, the actually measured instantaneous maximum value $U_{J,c,max}$, as shown by the black solid curve in figure 14($a$), is smaller than the nominal maximum value because of the limitation of the present state-of-the-art technology of solenoid valves and the inertia of the air in the tube. As such, $dc$ in (5.2) should be replaced by an effective duty cycle $dc_e$, which is defined by

$$U_{J,c,max} = \frac{\overline{U_{J,c}}}{dc_e}. \tag{5.3}$$

As shown in figure 14($b$), with $\overline{U^*_{J,c}}^3/dc^2$ replaced by $\overline{U^*_{J,c}}^3/dc_e^2$, $dc$ and $dc_e$ are linearly correlated, *viz.*

$$dc_e = 0.95dc + 0.09. \tag{5.4}$$

Equation (5.4) differs from the correlation between $dc$ and $dc_e$ reported by Fan *et al.* (2023). This deviation may result from the different systems producing the pulsed jet. In their study, the minijet from the solenoid valve is directly injected into the main jet, while the present pulsed jet first flows into an actuator chamber after the solenoid valve (figure 1$b$) and then is injected into the mainstream.

We now use $\overline{U^*_{J,c}}^3/dc_e^2$ as the abscissa and then observe that the correlation between $(\Delta\overline{C_{p,e}})_{opt}$ and $\overline{U^*_{J,c}}^3/dc_e^2$ overlaps reasonably well with that between $(\Delta\overline{C_{p,e}})_{opt}$ and $\gamma$ (figure 15). Note that the premise of (5.2) is that the time history of the jet velocity follows the square wave, which is achievable only at a low excitation frequency. At a high frequency, the time history of the jet velocity cannot be approximated as a square



https://doi.org/10.1017/jfm.2025.10797 Published online by Cambridge University Press

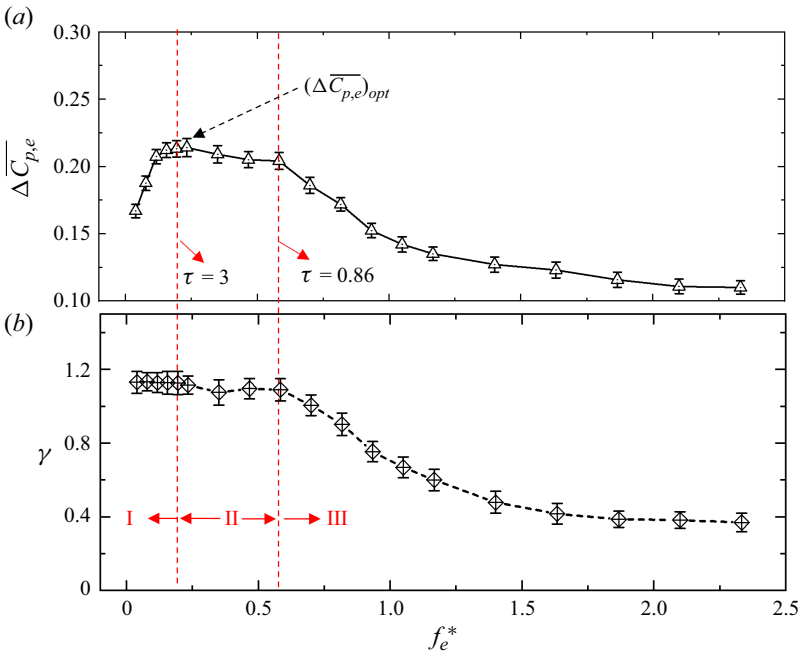



Figure 16. Dependence on $f_e^*$ of (*a*) $\Delta\overline{C_{p,e}}$ and (*b*) $\gamma$ ($\overline{U_{J,c}^*} = 0.72$, $dc = 0.5$, $\alpha = 0°$). The error bars denote the standard deviation out of 10 repeated measurements. The vertical red broken lines indicate a division that separates regions I and II or II and III.

wave and $\gamma$ cannot be written as $\overline{U_{J,c}^*}^3/dc_e^2$. Two important inferences can be made from figure 15. First, the scaling factor $\gamma$ is equivalent to $\overline{U_{J,c}^*}^3/dc_e^2$ at a low excitation frequency. This is because the time history of the jet velocity at a low frequency can be approximated as a square wave and $dc_e$ and $dc$ are linearly correlated (figure 14). Second, while a great amount of hotwire data is required to determine $\gamma$, $\overline{U_{J,c}^*}^3/dc_e^2$ can be directly calculated from the control parameters and (5.4). As found by Perumal & Zhou (2018), scaling factor $\overline{U_{J,c}^*}^3/dc_e^2$ is important in engineering applications, which can be used to predict $(\Delta\overline{C_{p,e}})_{opt}$ or to determine the control parameters.

### 5.2. *Analysis of $f_e^*$ and $\alpha$*

The scaling shown in figures 13 or 15 is obtained at $f_e^* = 0.23$. One may wonder whether $\Delta\overline{C_{p,e}}$ would also collapse when excitation frequency varies, with $\gamma$ remaining as the scaling factor. Figure 16 presents the variation in $\gamma$ and $\Delta\overline{C_{p,e}}$ with excitation frequency at $dc = 0.5$ and $\overline{U_{J,c}^*} = 0.72$. In regions II and III, the dependence of $\gamma$ on excitation frequency exhibits excellent similarity to that of $\Delta\overline{C_{p,e}}$. Furthermore, the critical $\tau$ where region II changes to region III is 0.86, the same as in figure 5. However, the variations in $\gamma$ and $\Delta\overline{C_{p,e}}$ with excitation frequency display a marked difference in region I; $\Delta\overline{C_{p,e}}$ rises rapidly with excitation frequency, whilst $\gamma$ varies little. The result suggests that the way excitation frequency influences $\Delta\overline{C_{p,e}}$ in regions II and III may result, via the relation between $\Delta\overline{C_{p,e}}$ and $\gamma$ (figures 13 or 15), from the variation in $\gamma$ with excitation frequency, whereas in region I, there may be other controlling factors at play besides $\gamma$.



https://doi.org/10.1017/jfm.2025.10797 Published online by Cambridge University Press

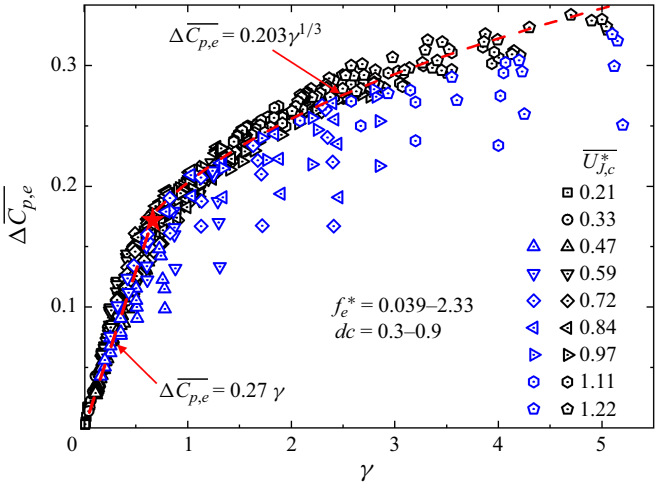



Figure 17. Dependence of $\Delta\overline{C_{p,e}}$ on $\gamma$ ($\alpha = 0°$), including all data points in figures 5 and 6(*a*,*b*). The blue and black symbols denote data points in region I ($\tau > 3$) and regions II, III ($\tau \leq 3$), respectively. The latter fall around a red broken curve, which is the least-squares-fitting curve to the data.

The above-mentioned speculation is indeed confirmed. Figure 17 presents the dependence of $\Delta\overline{C_{p,e}}$ on $\gamma$, including all the data at $\alpha = 0°$ in figure 5(*a*,*b*) and 6. All of the data points in regions II and III collapse well about the red broken curve, but not those in region I, as shown by the blue symbol, which shows a large departure from the curve. This result points unequivocally to the fact that in contrast to regions II and III, $\Delta\overline{C_{p,e}}$ depends not only on $\gamma$, but also on other factors. This observation raises two issues. One is why $\gamma$ exhibits little dependence on excitation frequency in the low frequency range, or regions I and II (figure 16), but drops with rising excitation frequency in the high frequency range, or region III. The other is what factors, apart from $\gamma$, play a non-negligible role in region I.

To address the first issue, let us take a close look at the data of jet velocity at $dc = 0.5$ and $\overline{U_{J,c}^*} = 0.72$. Figure 18(*a*) presents the variations with excitation frequency in the root mean square (r.m.s.) value $U_{J,c}'^*$ of the jet velocity (left ordinate) and the corresponding $\gamma$ (right ordinate). The two curves are almost parallel to each other; $U_{J,c}'^*$ and $\gamma$ display a small variation with excitation frequency at $f_e^* \leq 0.58$ or $\tau \geq 0.86$ (regions I and II) but both drop and then eventually level off at $f_e^* > 0.58$ (region III). Figure 18(*b*) shows the phase-averaged time histories of the jet velocity at five representative frequencies, i.e. $f_e^* = 0.04$, 0.23, 0.58, 1.17, 2.33. The time $t$ is normalised by the period $T$ of the pulsed jet. The time histories are approximately square waves at $f_e^* = 0.04$, 0.23 and 0.58, and their maximum and minimum values are almost the same. As excitation frequency increases beyond $f_e^* = 0.58$, the time history changes from a square-wave-like to a sinusoidal-wave-like signal at $f_e^* = 1.17$ or 2.33. The corresponding maximum value drops, while the minimum value rises markedly, thus leading to a reduced magnitude in the jet velocity or $\gamma$. In summary, the time history of the jet velocity is approximately a square wave in regions I and II ($\tau \geq 0.86$), and the corresponding maximum, minimum and r.m.s. values vary little for different excitation frequencies. Consequently, $\gamma$ is independent of excitation frequency and can be rewritten as $\overline{U_{J,c}^*}^3/dc_e^2$, as shown in figure 14. In region III ($\tau < 0.86$), the variation in r.m.s. value or time history of the jet velocity with excitation



https://doi.org/10.1017/jfm.2025.10797 Published online by Cambridge University Press

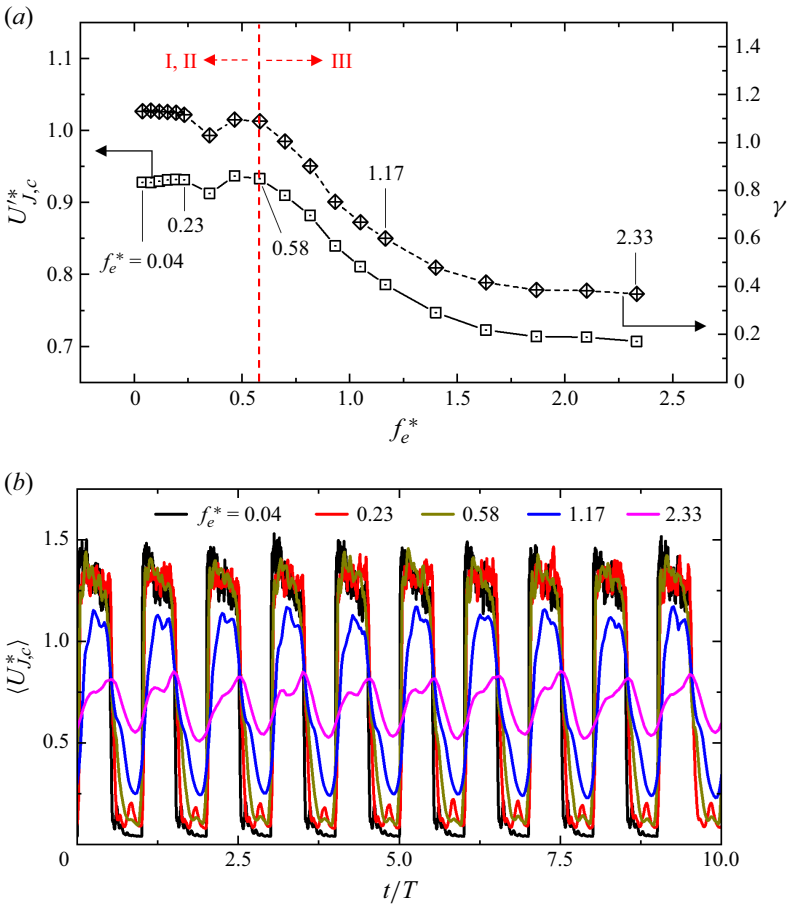



Figure 18. (*a*) Dependence on $f_e^*$ of $U'^*_{J,c}$ and $\gamma$; (*b*) time histories of $\langle U^*_{J,c} \rangle$ at different $f_e^*$ ($dc = 0.5$, $\overline{U^*_{J,c}} = 0.72$).

frequency results in a change in $\gamma$, which is responsible for the decrease in $\Delta\overline{C_{p,e}}$ with excitation frequency (figure 5).

The jet exit velocity generated in experiments may change from the characteristics of a square wave to those of a sinusoidal wave with increasing excitation frequency due to viscous losses and jet inertia (Barros *et al.* 2014, 2016), and accordingly, its magnitude diminishes as well. It is further found that the frequency, where the wave shape starts to show appreciable change, varies with the duty cycle, but $\tau$ would not. The present critical $\tau$ of 0.86 may depend on the system that generates the pulsed jet, including the position and response time of the solenoid valve in the supply line, the design of plenum and so on. In their numerical investigation on wing circulation control, Liu *et al.* (2004) found that the square wave was more effective than the sinusoidal wave. Given a lift coefficient, the required mass flow rate for the sinusoidal pulsed jet was much higher than that for the square-wave jet. This is, as shown in figure 18, because a square-wave jet is associated with a higher $\gamma$ than a sinusoidal wave jet, even under the same mass flow rate.

To address the second issue, we carefully analyse the data points in region I (blue symbols in figure 17), which exhibit a significant departure from those in regions II and III. It is found that once $\Delta\overline{C_{p,e}}$ is rescaled by $\Pi(\tau)$, as shown in figure 19,



https://doi.org/10.1017/jfm.2025.10797 Published online by Cambridge University Press

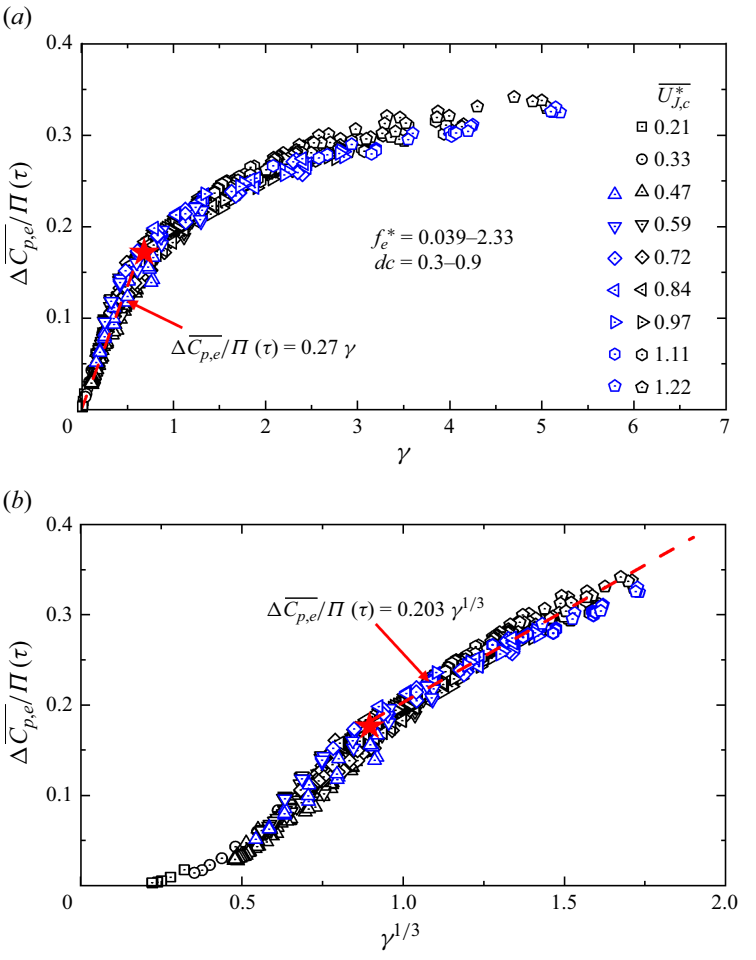



Figure 19. Dependence of $\Delta\overline{C_{p,e}}/\Pi(\tau)$ on (*a*) $\gamma$ ($\alpha = 0°$, $\gamma < 0.7$) and (*b*) $\gamma^{1/3}$ ($\gamma \geq 0.7$), where the red dashed curve is the least-squares fitting to data points. The blue and black symbols denote data points in region I ($\tau > 3$) and regions II, III ($\tau \leq 3$), respectively. The red star, corresponding to the red star in figure 4, represents the critical point where the separation bubble disappears.

all data points at various $\overline{U^*_{J,c}}$, $dc$ and $f_e^*$ collapse well about a piecewise least-square fitting curve, *viz.*

$$\Delta\overline{C_{p,e}}/\Pi\,(\tau) = \begin{cases} 0.27\gamma, & \gamma < 0.7, \\ 0.203\gamma^{1/3}, & \gamma \geq 0.7, \end{cases} \tag{5.5}$$

where $\Pi(\tau)$ is a function of $\tau$, given by

$$\Pi\,(\tau) = \begin{cases} 1, & \tau \leq 3, \\ -0.021\tau + 1.06, & \tau > 3. \end{cases} \tag{5.6}$$

When $\tau > 3$ (region I), $\Pi(\tau) \neq 1$ and $\Delta\overline{C_{p,e}}$ (blue symbols) depend on not only $\gamma$ but also $\tau$ or $\Pi(\tau)$; when $\tau \leq 3$ (regions II and III), $\Pi(\tau) \equiv 1$ and $\Delta\overline{C_{p,e}}$ (black symbols) depend only on $\gamma$ since $\tau$ is so small that its effect may be neglected. It is noteworthy that the data points in region I of figure 17 scatter rather wildly because the presented $\Delta\overline{C_{p,e}} = f\,(\gamma)$ does not include the possible effect of $\tau$.



https://doi.org/10.1017/jfm.2025.10797 Published online by Cambridge University Press

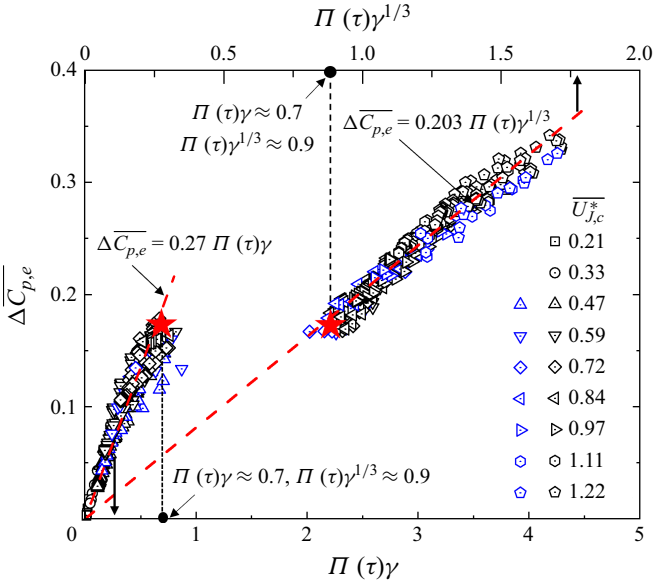



Figure 20. Dependence of $\Delta\overline{C_{p,e}}$ on $\Pi(\tau)\gamma$ and $\Pi(\tau)\gamma^{1/3}$ ($\alpha = 0°$). The red dashed lines are the least-squares fitting to data points. The red star is the same as in figure 19.

The relation '$\Delta\overline{C_{p,e}}/\Pi(\tau) = f_2(\gamma)$' in figure 19 may be rewritten as $\Delta\overline{C_{p,e}} = \Pi(\tau) f_2(\gamma)$. As shown in figure 20, $\Delta\overline{C_{p,e}}$ can be then divided into two regimes, i.e. $\Delta\overline{C_{p,e}} = 0.27\Pi(\tau)\gamma$ for $\Pi(\tau)\gamma < 0.7$ and $\Delta\overline{C_{p,e}} = 0.203\Pi(\tau)\gamma^{1/3}$ for $\Pi(\tau)\gamma \geq 0.7$, corresponding to before and after the disappearance of the separation bubble. Apparently, $\Pi(\tau)$ is physically an indicator for the control efficiency which depends on only $\tau$.

Insight may be gained into how $\tau$ may affect $\Delta\overline{C_{p,e}}$ in region I by the analysis of the time histories of $\langle C_{p,e}\rangle$ along with $\langle U^*_{J,c}\rangle$. Consider two different combinations of $\tau$ and $\Pi(\tau)$ in figure 21, i.e. case 1 ($\tau = 12.8$, $\Pi(\tau) = 0.79$) from region I and case 2 ($\tau = 2.2$, $\Pi(\tau) = 1$) from region II. The time histories of $\langle U^*_{J,c}\rangle$ are square-wave-like, and display a reasonably good overlap in terms of the jet-on and -off durations for the two cases when normalised by the period $T$ of the pulsed jet (figure 21*a*). Their peaks and valleys are comparable, thus producing the same $\gamma$ ($= 1.13$), which facilitates the study of the effect of $\tau$ on $\Delta\overline{C_{p,e}}$. The time histories of $\langle C_{p,e}\rangle$ for the two cases are characterised by approximately the same peak value but very different troughs (figure 21*b*). With a small $\tau$, case 2 features a higher trough value than case 1, thus a larger $\Delta\overline{C_{p,e}}$. When the jet is turned off and $\langle U^*_{J,c}\rangle$ falls, $\langle C_{p,e}\rangle$ starts to drop and finally reaches its trough. When the jet is turned on again, with $\langle U^*_{J,c}\rangle$ rising, in the next cycle of the jet, $\langle C_{p,e}\rangle$ rises and reaches the peak at the end of a duration $dc/f^*_e$. In case 1, $\langle C_{p,e}\rangle$ descends to a value comparable to the baseline flow due to a larger $\tau$ ($= 12.8$), suggesting flow separation again and the Coanda effect disappears almost completely before the next cycle. In case 2, once the jet is off, $\langle C_{p,e}\rangle$ also drops but could not reach the same trough as the baseline flow because of a small $\tau$ ($= 2.2$). Consequently, flow separation is always suppressed, at least partially, during the entire excitation period. Then, it seems plausible that a sufficiently small $\tau$, i.e. in regions II and III where $\tau \leq 3$, may take advantage of jet inertia to sustain continuously the Coanda effect, thus maintaining $C_{p,e}$ at a higher level even when the jet is turned off. If a new blowing cycle starts under such circumstances, the Coanda effect may immediately recover itself towards the optimal state achievable for a given jet energy. This physical



https://doi.org/10.1017/jfm.2025.10797 Published online by Cambridge University Press

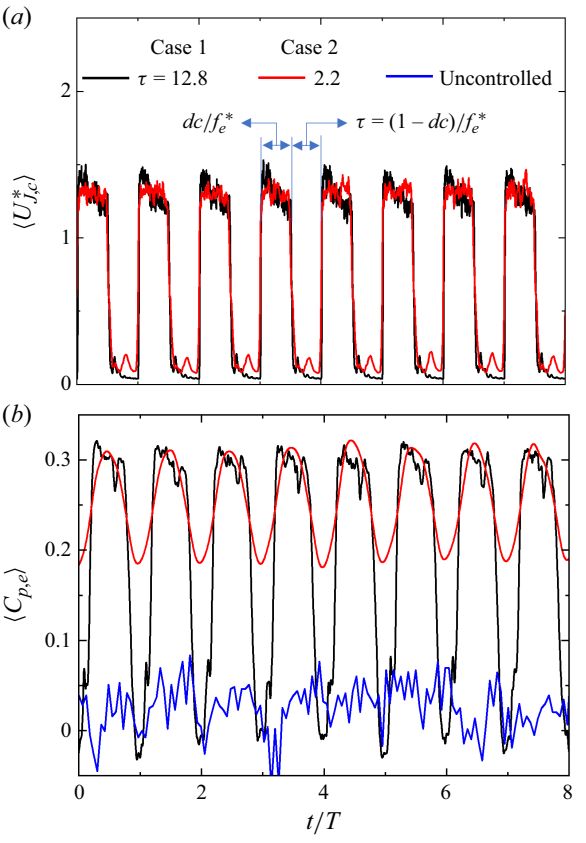



Figure 21. Time histories of (*a*) $\langle U^*_{J,c}\rangle$ and (*b*) corresponding $\langle C_{p,e}\rangle$ for $\tau = 12.8$ and 2.2 ($\alpha = 0°$, $\overline{U^*_{J,c}} = 0.72$, $dc = 0.5$), along with the uncontrolled case.

process underpins the rapid rise in $\Delta\overline{C_{p,e}}$ with increasing excitation frequency in region I (figure 5).

The scaling analysis shown in figure 19 is obtained at $\alpha = 0°$. As shown in figure 22, a similar collapse is observed at $\alpha = 25°$ and 55° when the data are plotted against $\gamma$. Given $\gamma$, the smaller the $\alpha$, the larger the $\Delta\overline{C_{p,e}}$, which reaches the maximum at $\alpha = 0°$. One may wonder whether a scaling law is present even when $\alpha$ varies. After careful analysis along with numerous trial-and-error attempts, it is found that $\Delta\overline{C_{p,e}}/\Pi(\tau)$ of all $\alpha$ collapse around a curve provided that $\gamma$ in figure 22 is replaced by $\xi$ (figure 23), *viz.*

$$\Delta\overline{C_{p,e}}/\Pi(\tau) = \begin{cases} 0.27\xi, & \xi < 0.7, \\ 0.203\xi, & \xi \geq 0.7, \end{cases} \tag{5.7}$$

where the scaling factor $\xi$ is defined by

$$\xi = \overline{U^{*3}_{J,c,t}} \tag{5.8}$$

and

$$U^*_{J,c,t} = U^*_{J,c}\cos\alpha = \frac{U_{J,c}\cos\alpha}{U_\infty}. \tag{5.9}$$



https://doi.org/10.1017/jfm.2025.10797 Published online by Cambridge University Press

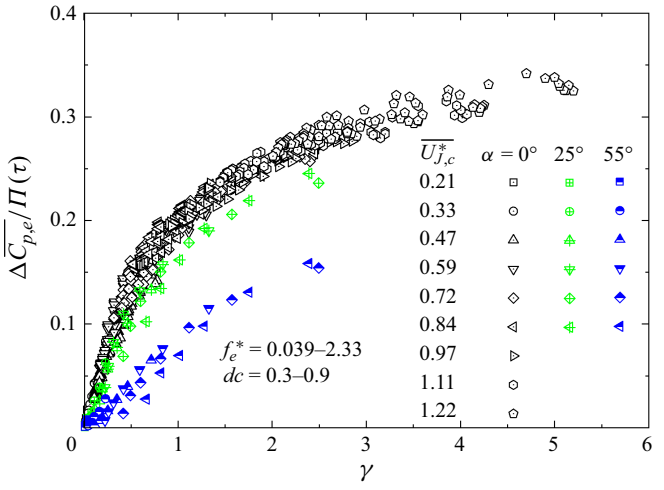



Figure 22. Dependence of $\Delta\overline{C_{p,e}}/\Pi(\tau)$ on $\gamma$ for various α.

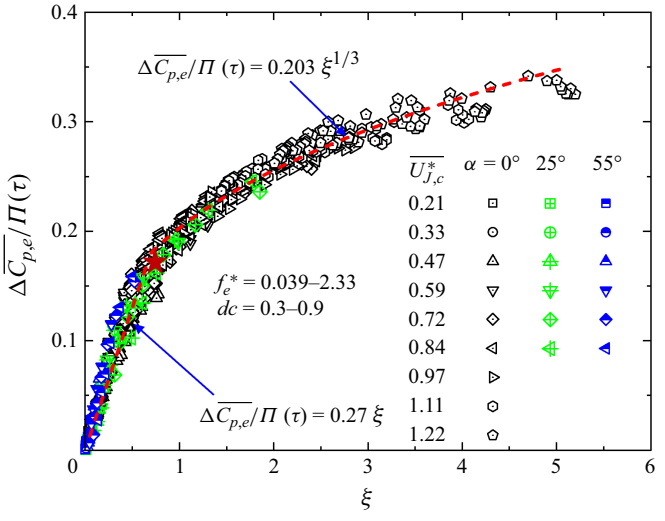



Figure 23. Dependence of $\Delta\overline{C_{p,e}}/\Pi(\tau)$ on $\xi$, where the red broken curve is the least-squares fitting to the measured data. The red star is as in figure 20.

Equation (5.7) is the same in form as (5.5), including the turning point position.

### 5.3. *Relationship between steady and pulsed jet controls and $Re_\theta$ effect*

He *et al.* (2023) manipulated the same flow using a steady blowing jet. One may naturally wonder whether the scaling law (5.7) could be applied to the case of steady control since the unsteady control approaches steady when excitation frequency becomes very large, as suggested by figure 18(*b*). Figure 24(*a*) presents the dependence of $\Delta\overline{C_{p,e}}$ on $\overline{U^*_{J,c}}$ and $Re_\theta$ (=5700−12 200) using a steady control jet at $\alpha = 0°$ and 25°. As found by He *et al.* (2023), the data points at different $Re_\theta$ collapse reasonably well about a curve for a given jet angle if plotted against $\overline{U^*_{J,c}}$. Interestingly, the data points from steady jet control collapse well with the present data under the pulsed jet control, irrespective of $\alpha$ and $Re_\theta$, when $\xi$



https://doi.org/10.1017/jfm.2025.10797 Published online by Cambridge University Press

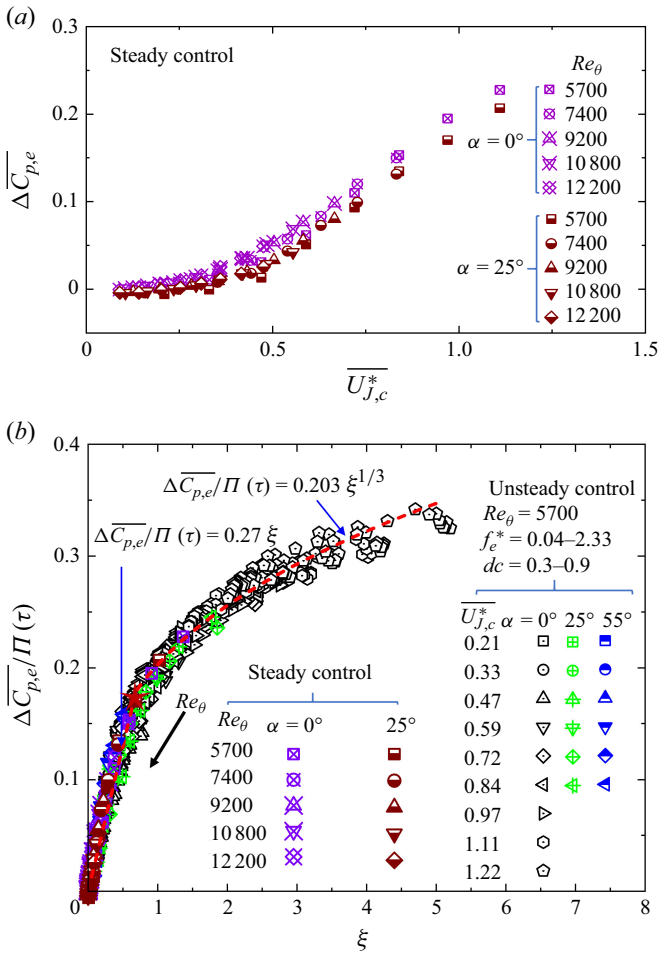



Figure 24. (*a*) Dependence of $\Delta\overline{C_{p,e}}$ on the velocity ratio $\overline{U^*_{J,c}}$ of steady jet control at various $Re_\theta$. The data of steady control at $\alpha = 25°$ are from He *et al.* (2023) and those of $\alpha = 0°$ are the present data; (*b*) dependence of $\Delta\overline{C_{p,e}}/\Pi(\tau)$ on $\xi$, including the data of both steady and pulsed jet controls, where the red dashed curve is the least-squares fitting to the measured data. The red star is the same as in figures 19 and 23.

is used as the scaling factor (figure 24*b*). The observation suggests that the scaling law is applicable for not only pulsed jet control but also steady jet control. The latter is a special case of the former, where $\tau = 0$, $\Pi(\tau) = 1$ in (5.6) and $\xi = \overline{U^{*3}_{J,c,t}} = \overline{U^*_{J,c,t}}^3$ ($\xi = \overline{U^{*3}_{J,c,t}} \neq \overline{U^*_{J,c,t}}^3$ for a pulsed control jet). As a result, this scaling law can be simplified to $\Delta\overline{C_{p,e}} = f_3(\overline{U^*_{J,c}})$ for a steady control jet at a given jet angle, as found by He *et al.* (2023). As another note, although the data of $\Delta\overline{C_{p,e}}$ against $\overline{U^*_{J,c}}$ display a quite good collapse about a curve in figure 24(*a*), the scaling law shown in figure 24(*b*) contains richer information on top of its broader applicability. Take the turning point marked by a star in figure 24(*b*) for example. This point corresponds to the control state where the separation bubble just disappears. The pressure recovers rapidly and linearly with $\xi$ before reaching this point due to a contraction in the separation bubble size, but slowly beyond this point.



https://doi.org/10.1017/jfm.2025.10797 Published online by Cambridge University Press

It is well known that $\Delta\overline{C_{p,e}}$ depends on $\overline{U^*_{J,c}}$, d$c$, $f^*_e$, $\alpha$ and $Re_\theta$ i.e.

$$\Delta\overline{C_{p,e}} = f_1\big(\overline{U^*_{J,c}}, dc, f^*_e, \alpha, Re_\theta\big). \tag{5.10}$$

As shown in figure 24(*b*), this highly complex relationship is now reduced to

$$\Delta\overline{C_{p,e}}/\Pi(\tau) = f_2(\xi). \tag{5.11}$$

This scaling law provides not only valuable insight into the flow physics behind control, but also important guidance for the choice of control parameters and the prediction of control performance. First, this scaling law may be written as $\Delta\overline{C_{p,e}} = 0.27\Pi(\tau)\xi$ and $0.203\Pi(\tau)\xi^{1/3}$, corresponding to before and after the disappearance of the separation bubble, respectively. We see immediately that the factor $0.27\Pi(\tau)$ can be understood to be the end pressure coefficient rise for each unit energy input associated with the tangential jet velocity $U^*_{J,c,t}$, that is, $\Pi(\tau)$ is an indicator of the control efficiency. Second, the duration $\tau$ plays an important role in determining the control performance. Here, $\Pi(\tau)$ is a function of $\tau$. In regions II and III, $\tau$ ($\leq 3$) is so small that its effect on $\Delta\overline{C_{p,e}}$ can be neglected. Thus, $\Pi(\tau) \equiv 1$ and $\Delta\overline{C_{p,e}}$ depends only on $\xi$ (figures 19 and 20). In region I, $\tau > 3$ and $\Pi(\tau)$ drops linearly with increasing $\tau$ ( 5.6) and $\Delta\overline{C_{p,e}}$ depends not only on $\xi$ but also on $\tau$ (figures 19 and 20), and a larger $\tau$ will result in a smaller $\Delta\overline{C_{p,e}}$ for a fixed $\xi$ (figure 21). Third, the optimal control strategy is that the jet is injected tangentially, i.e. at $\alpha = 0°$ (figure 22), and at $\tau = 0.86$–3, i.e. in region II (figure 5). For tangential jet control in region II where $\xi = \gamma = \overline{U^*_{J,c}}^3/dc_e^2$ holds, given $\overline{U^*_{J,c}}$ and $dc$, $\overline{U^*_{J,c}}^3/dc_e^2$ may be directly calculated and hence $\Delta\overline{C_{p,e}}$ can be predicted from (5.7). This may have important applications in engineering. Conversely, the required $\overline{U^*_{J,c}}$ to achieve a pre-specified $\Delta\overline{C_{p,e}}$, say $\Delta\overline{C_{p,e}} \approx 0.17$ where the separation bubble vanishes completely, can be estimated from $\overline{U^*_{J,c}}^3/dc_e^2$ based on (5.7), which is approximately 0.4 at $dc_e = 0.3$, 50 % lower than that ($\overline{U^*_{J,c}} = 0.8$) at $dc_e = 0.9$. Clearly, the required $\overline{U^*_{J,c}}$ drops with a decreasing $dc$. The mass flow rate or $\overline{U^*_{J,c}}$ is practically an important factor. Fourth, we may gain understanding from this law on the effect of $Re_\theta$ on $\Delta\overline{C_{p,e}}$, other than parameters $\overline{U^*_{J,c}}$, $dc$, $f^*_e$ and $\alpha$. This effect is linked to how a variation in $Re_\theta$ may change $\xi$. Given the same $\xi$, $\Delta\overline{C_{p,e}}$ will be the same, irrespective of a different $Re_\theta$. Fifth, when $\Pi(\tau) = 1$ and $\xi$ is fixed, $\Delta\overline{C_{p,e}}$ will be the same at a given jet angle, whether under steady or unsteady control. The pulsed jet can produce a higher $\xi$ at a given jet angle because the same mass flow is injected into the mainstream at a higher velocity. This explains why the pulsed control jet can achieve the same $\Delta\overline{C_{p,e}}$ at a smaller mass flow rate compared with the steady jet, or can achieve higher $\Delta\overline{C_{p,e}}$ at the same mass flow rate. The reduction in mass flow rate for the pulsed jet can be quantitatively calculated by $\overline{U^*_{J,c}}^3/dc_e^2$. The effective duty cycle $dc_e$ is 1 for a steady control jet. Finally, one remark is due. We have applied the present scaling law to the data obtained from flow around an axisymmetric body, supported on an aerofoil strut, which is manipulated using eight synchronised tangential unsteady jets. The integrated values of the pressure coefficient $\overline{C_p}$ around the curved surface of after-body, measured at different d$c$, $f^*_e$ and $\overline{U^*_{J,c}}$, exhibit a surprising collapse, suggesting the validity of this scaling law even for a three-dimensional body. It could be interesting to validate this scaling law for other curved ramp flows in future work.



https://doi.org/10.1017/jfm.2025.10797 Published online by Cambridge University Press

## 6. Net power saving and control efficiency

Net power saving rate $S_n$ and control efficiency $\eta$ are the key indicators for successful control and are defined by

$$S_n = \frac{\Delta\overline{F_D}U_\infty - P_j}{\overline{F_{D0}}U_\infty}, \tag{6.1}$$

$$\eta = \frac{\Delta\overline{F_D}U_\infty}{P_j}, \tag{6.2}$$

where $P_j$ is the jet power, $\Delta\overline{F_D} = \overline{F_D} - \overline{F_{D0}}$ is the drag reduction under control, and $\overline{F_D}$ and $\overline{F_{D0}}$ represent the time-averaged drag forces on the ramp with and without control, respectively. Following Hlevca *et al.* (2018), $F_D$ is calculated by integrating the streamwise component of the force due to the pressure difference, *viz.*

$$F_D = \int\int_s (P - P_\infty)\sin\beta \, \mathrm{d}s, \tag{6.3}$$

where d$s$ is the surface element of the ramp surface, and $\beta$ is the angle between the local tangent direction of the ramp and the streamwise direction, which is a function of $x$ and can be determined from the equation that governs the ramp contour. Here, $P_j$ is calculated by

$$P_j = \int_{-\frac{l}{2}}^{\frac{l}{2}}\int_{-x_0'}^{x_0'} \left[\overline{\left|0.5\rho U_J^3\right|} + \overline{\left|\Delta P_w U_J\right|}\right] \mathrm{d}x' \, \mathrm{d}z', \tag{6.4}$$

where $l$ is the spanwise length of the slit through which the jet issues and $\Delta P_w$ is the pressure difference that drives the jet through the slit. As demonstrated in figure 2($d$), the distribution of $U_J$ along the $x'$ direction is assured as a parabolic profile (Cheng *et al.* 2021; Zhang *et al.* 2022) and may be determined from

$$\frac{U_J}{U_{J,c}} = 1 - \left(\frac{x'}{x_0'}\right)^2. \tag{6.5}$$

We calculate $S_n$ and $\eta$ from (6.1)–(6.2) at $\alpha = 0°$, where the optimal control performance is achieved, and present the solutions in figure 25. The blue area represents all $S_n$ and $\eta$ values feasible with the present control system or the feasibility domain, which occurs in the first, second and third quadrants. The black solid circle is a critical point where $S_n = 0$ and $\eta = 1$. On its left (the second and third quadrants) where $\eta < 1$, the control is ineffective due to $S_n < 0$. The control is effective on its right or in the first quadrant ($\eta > 1$), where the power saving due to drag reduction is more than the consumed control energy ($S_n > 0$). The red solid curve may be referred to as the Pareto frontier (Lewis, Tackett & Mattson 2014) or optimal solution set. There is no solution within the feasibility domain, whose $S_n$ and $\eta$ are simultaneously greater than the values on the Pareto frontier. Moving upward along the right border (the red dashed line) of the feasible domain, $S_n$ remains constant, while $\eta$ rises rapidly. This implies that the required control energy is reduced for the same $S_n$. Ascending further along the Pareto frontier from the turning point marked by the red star, $S_n$ retreats very quickly, though $\eta$ continues rising at a much slower rate. Consequently, from the point of power consumption, the turning point can be considered as the optimal solution. Note that $\Delta\overline{C_{p,e}} = 0.17$ at this turning point, corresponding exactly to the turning point in figures 4, 19, 23 and 24. This optimal solution leads to $S_n = 40\,\%$ and $\eta = 3.5$. The thick yellow dashed curve with arrows indicates the



https://doi.org/10.1017/jfm.2025.10797 Published online by Cambridge University Press

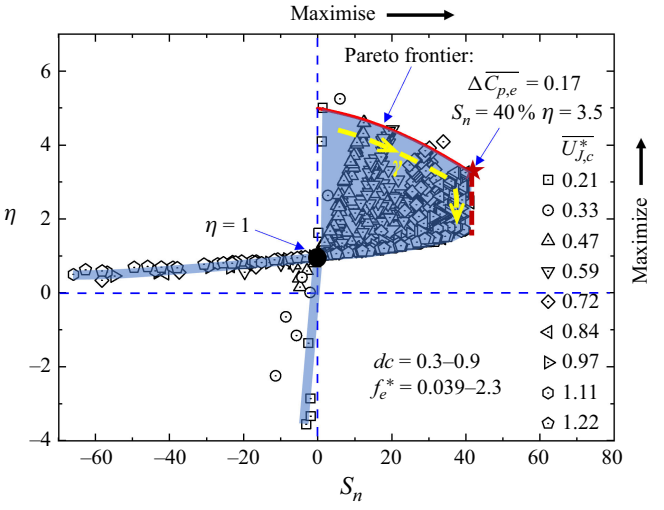



Figure 25. Correlation between the net saving energy rate $S_n$ and control efficiency $\eta$ ($\alpha = 0°$), where the blue area represents the feasibility domain. The black circle is the critical point where $S_n = 0$ and $\eta = 1$; the red solid curve is the Pareto frontier (the optimal solution set); the red dashed line is the right border of the feasibility domain; the yellow dashed curve with an arrow indicates the increasing direction of $\gamma$ along the Pareto frontier; the red star denotes the optimal control where the maximum $S_n$ is associated with the maximum $\eta$ achievable, corresponding to the point marked by the red star in figures 4, 19, 23 and 24.

increasing direction of $\gamma$ along the border of the feasibility domain. Let us discuss this result in conjunction with figure 20. Given $\Pi(\tau) = 1$, $\Delta\overline{C_{p,e}}$ rises rapidly and linearly with increasing $\gamma$. The corresponding separation bubble contracts and $S_n$ keeps rising, though $\eta$ declines slowly. The optimal control where the maximum $S_n$ is associated with the maximum $\eta$ is achieved when the separation bubble just disappears and the dependence of $\Delta\overline{C_{p,e}}$ on $\gamma$ reaches the turning point. As $\gamma$ increases further beyond this point, $\Delta\overline{C_{p,e}}$ continues to rise at a smaller rate. Then, $S_n$ does not increase anymore and $\eta$ drops rapidly.

## 7. Conclusions

Flow separation from a curved ramp is manipulated using a spanwise pulsed slit jet. Four control parameters are investigated, i.e. mean velocity ratio $\overline{U^*_{J,c}}$, duty cycle $dc$, pulsed dimensionless frequency $f_e^*$ and jet blowing angle $\alpha$. The Reynolds number $Re_\theta$ based on the momentum thickness is 5700. The following conclusions may be drawn out of this work.

(i) The control physics and performance are very different at small $\alpha(\leq 55°)$ from their counterparts at large $\alpha(>55°)$. The pulsed jet with a large $\alpha$ produces two effects. First, the upward jet injects momentum into incident shear layer and acts to enlarge the separation bubble, as observed under steady jet control (He *et al.* 2023). Second, the jet generates spanwise vortices, acting to enhance momentum transfer and reduce the separation bubble. When the excitation frequency coincides with the natural vortex shedding frequency, the spanwise vortices are strengthened, causing a slight contraction in the separation bubble. However, at a small $\alpha$, the tangential component of the jet induces a Coanda effect, producing a low-pressure region near the wall. The pressure difference between the main stream and the near wall flow pushes



https://doi.org/10.1017/jfm.2025.10797 Published online by Cambridge University Press

the separated flow towards the wall. As a result, the recirculation bubble may be completely eliminated, resulting in substantial pressure recovery.

(ii) The control performance, as indicated by the value of $\Delta\overline{C_{p,e}}$ (figure 4), depends strongly on $\alpha$ ($\alpha \leq 55°$), $\overline{U^*_{J,c}}$, $f^*_e$ and $dc$, i.e. $\Delta\overline{C_{p,e}} = f_1(\overline{U^*_{J,c}}, \mathrm{d}c, f^*_e, \alpha)$. It has been found from empirical scaling analysis that this complex relationship may be reduced to $\Delta\overline{C_{p,e}}/\Pi(\tau) = f_2(\xi)$ (figure 23). The parameter $\Pi(\tau)$ is a function of the duration $\tau$ (figures 19–21). The scaling factor $\xi$ is physically the energy ratio pre unit area of the control jet to mainstream. Here, $\Delta\overline{C_{p,e}}$ is given by $0.27\Pi(\tau)\xi$ in the presence of the separation bubble and by $0.203\Pi(\tau)\xi^{1/3}$ after the separation bubble disappears. Given $\xi$, $\Delta\overline{C_{p,e}}/\Pi(\tau)$ is the same, irrespectively of the combination of $\overline{U^*_{J,c}}$, $dc$, $f^*_e$ and $\alpha$. In regions II and III ($\tau \leq 3$), $\Pi(\tau) \equiv 1$ and $\Delta\overline{C_{p,e}}$ depends only on $\xi$ (figures 17 and 23). In region I ($\tau > 3$), $\Pi(\tau) \neq 1$ and $\Delta\overline{C_{p,e}}$ depends not only on $\xi$ but also on $\tau$ (figures 19, 23). The scaling law provides not only valuable insight into the flow physics behind control, but also an important guidance for the choice of control parameters.

(iii) Several interesting inferences can be obtained from the scaling law. First, this law is also applicable to steady jet control (figure 24), which is a special case, i.e. $\xi = \overline{U^{*3}_{J,c,t}} = \overline{U^*_{J,c,t}}^3$ and $\tau = 0$, of pulsed jet control. As a result, this law can be simplified to $\Delta\overline{C_{p,e}} = f_3(\overline{U^*_{J,c}})$ for a steady jet at a given $\alpha$, as found by He *et al.* (2023). Second, the dependence of $\Delta\overline{C_{p,e}}$ on $Re_\theta$ is linked to how a variation in $Re_\theta$ may change $\xi$. Given the same $\xi$, $\Delta\overline{C_{p,e}}$ will be the same, irrespective of different $Re_\theta$. That is, $\Delta\overline{C_{p,e}} = f_1(\overline{U^*_{J,c}}, \mathrm{d}c, f^*_e, \alpha, Re_\theta)$ may be reduced to $\Delta\overline{C_{p,e}}/\Pi(\tau) = f_2(\xi)$. Third, assuming $\Pi(\tau) = 1$ and a fixed $\xi$, $\Delta\overline{C_{p,e}}$ will be the same at a given $\alpha$, be steady or unsteady control jet. Given the same jet energy ratio, the required $\overline{U^*_{J,c}}$ is much smaller for a pulsed jet than for a steady jet, which may have an important implication in practical engineering.

(iv) Given $\Pi(\tau) = 1$, $\Delta\overline{C_{p,e}}$ rises rapidly and linearly with increasing $\gamma$. The corresponding separation bubble contracts and the net energy saving rate $S_n$ keeps rising, though the control efficiency $\eta$ declines slowly. The optimal control, where the maximum $S_n$ is associated with the maximum $\eta$, is achieved when the separation bubble just disappears and the dependence of $\Delta\overline{C_{p,e}}$ on $\gamma$ displays an inflection point, the corresponding maximum $S_n$ and $\eta$ being 40 % and 3.5, respectively. Beyond the inflection point, $\Delta\overline{C_{p,e}}$ continues to rise with increasing $\gamma$, albeit at a smaller rate, though $S_n$ does not show any more increase and $\eta$ exhibits a more rapid decrease (figures 20 and 25), implying a deteriorating control efficiency.

**Funding.** Y.Z. wishes to acknowledge support given to him from NSFC through grant U24B2005.

**Declaration of interests.** The authors report no conflict of interest.

## References

Asgari, E. & Tadjfar, M. 2016 Assessment of four inflow conditions on large-eddy simulation of a gently curved backward-facing step. *J. Turbul.* **18**, 61–86.

Asgari, E. & Tadjfar, M. 2019 Active control of flow over a rounded ramp by means of single and double adjacent rectangular synthetic jet actuators. *Comput. Fluids* **190**, 98–113.

Asgari, E. & Tadjfar, M. 2022 Role of phase-difference between two adjacent rectangular synthetic jet actuators in active control of flow over a rounded ramp. *Phys. Fluids* **34**, 025101.

Bai, H.L., Zhou, Y., Zhang, W.G., Xu, S.J., Wang, Y. & Antonia, R.A. 2014 Active control of a turbulent boundary layer based on local surface perturbation. *J. Fluid Mech.* **750**, 316–354.



https://doi.org/10.1017/jfm.2025.10797 Published online by Cambridge University Press

BARROS, D., RUIZ, T., BORÉE, J. & NOACK, B.R. 2014 Control of a three-dimensional blunt body wake using low and high frequency pulsed jets. *Intern. J. Flow Control* **6**, 61–74.
BARROS, D., BORÉE, J., NOACK, B.R., SPOHN, A. & RUIZ, T. 2016 Bluff body drag manipulation using pulsed jets and coanda effect. *J. Fluid Mech.* **805**, 422–459.
BENTALEB, Y., LARDEAU, S. & LESCHZINER, M.A. 2012 Large-eddy simulation of turbulent boundary layer separation from a rounded step. *J. Turbul.* **13**, 1–28.
CHENG, X.Q., QIAO, Z.X., ZHANG, X., QUADRIO, M. & ZHOU, Y. 2021 Skin-friction reduction using periodic blowing through streamwise slits. *J. Fluid Mech.* **920**, A24.
CHIATTO, M., LUCA DE, L. & GRASSO, F. 2021 Modal analysis of actively controlled flow past a backward facing ramp. *Phys. Rev. Fluids* **6**, 064608.
DANDOIS, J., GARNIER, E. & SAGAUT, P. 2007 Numerical simulation of active separation control by a synthetic jet. *J. Fluid Mech.* **574**, 25–58.
DURIEZ, T., AIDER, J.-L. & WESFREID, J.E. 2008 Control of a separated flow over a smoothly contoured ramp using vortex generators. IUTAM Symposium on Flow Control and MEMS, vol. 7, pp. 437–441.
EATON, J.K. & SONG, S. 2004 Flow structures of a separating, reattaching, and recovering boundary layer for a large range of Reynolds number. *Exp. Fluids* **36**, 642–653.
EL-ASKARY, W.A. 2009 Turbulent boundary layer structure of flow over a smooth-curved ramp. *Comput. Fluids* **38**, 1718–1730.
EL SAYED, M.Y., SEMAAN, R. & RADESPIEL, R. 2017 Open loop control on a coanda flap water tunnel model. *AIAA Paper* 2017-3247
ENGLAR, R.J. 2000 Circulation control pneumatic aerodynamics: blown force and moment augmentation and modifications; past, present, and future. AIAA Paper 2000–2541
FAN, D. & ZHOU, Y. 2022 Scaling and classification of a minijet-manipulated turbulent jet. *Phys. Rev. Fluids* **7**, 074606.
GORTON, S., JENKINS, L. & ANDERS, S. 2002 Flow control device evaluation for an internal flow with an adverse pressure gradient. *AIAA Paper* 2002–0266
GREENBLATT, D., PASCHAL, K.B., YAO, C.-S. & HARRIS, J. 2006 Experimental investigation of separation control part 2: zero mass-flux oscillatory blowing. *AIAA J.* **44**, 2831–2845.
GUO, T., ZHONG, S. & CRAFT, T. 2020 Control of laminar flow separation over a backward-facing rounded ramp with c-d riblets – the effects of riblet height, spacing and yaw angle. *Int. J. Heat Fluid Fl.* **85**, 108629.
HAFFNER, Y., BORÉE, J., SPOHN, A. & CASTELAIN, T. 2020 Unsteady coanda effect and drag reduction for a turbulent wake. *J. Fluid Mech.* **899**, A36.
HE, S., ZHANG, K., SONG, Y. & ZHOU, Y. 2023 Control of flow separation from a curved ramp using a steady-blowing jet. *Phys. Fluids* **35**, 045139.
HLEVCA, D., GILLIÉRON, P. & GRASSO, F. 2018 Experimental study of the active control applied to the flow past a backward facing ramp. *Exp. Fluids* **59**, 39.
JONES, G.S., VIKEN, S.A., WASHBURN, A.E., JENKINS, L.N. & CAGLE, C.M. 2002 An active flow circulation controlled flap concept for general aviation aircraft applications. *AIAA Paper* 2002–3157
JONES, A., EDSTRAND, A., CHANDRAN, M., WETZEL, D., LIU, F. & CATTAFESTA, L. 2010 An experimental investigation of unsteady and steady circulation control for an elliptical airfoil. *AIAA Paper* 2010–346
JOSEPH, P., AMANDOLESE, X., EDOUARD, C. & AIDER, J.-L. 2013 Flow control using mems pulsed micro-jets on the ahmed body. *Exp. Fluids* **54**, 1442.
KOKLU, M. & OWENS, L.R. 2017 Comparison of sweeping jet actuators with different flow-control techniques for flow-separation control. *AIAA J.* **55**, 848–860.
LARDEAU, S. & LESCHZINER, M.A. 2011 The interaction of round synthetic jets with a turbulent boundary layer separating from a rounded ramp. *J. Fluid Mech.* **683**, 172–211.
LESCHZINER, M.A. & LARDEAU, S. 2011 Simulation of slot and round synthetic jets in the context of boundary-layer separation control. *Philos. Trans. A Math. Phys. Eng. Sci.* **369**, 1495–1512.
LEWIS, P.K., TACKETT, M.W. & MATTSON, C.A. 2014 Considering dynamic pareto frontiers in decision making. *Optim. Eng.* **15**, 837–854.
LI, Z., ZHANG, D., LIU, Y., WU, C. & GAO, N. 2020 Effect of periodic perturbations on the turbulence statistics in a backward-facing step flow. *Phys. Fluids* **32**, 075116.
LIM, H.D. & LYU, Z. 2021 Observations of a sweeping jet actuator for flow separation control of a backward-facing ramp. *Phys. Rev. Fluids* **6**, 043902.
LIU, Y., SANKAR, L.N., ENGLAR, R.J., AHUJA, K.K. & GAETA, R. 2004 Computational evaluation of the steady and pulsed jet effects on the performance of a circulation control wing section. *AIAA Paper* 2004–56
MA, X. & SCHRÖDER, A. 2017 Analysis of flapping motion of reattaching shear layer behind a two-dimensional backward-facing step. *Phys. Fluids* **29**, 115104.



https://doi.org/10.1017/jfm.2025.10797 Published online by Cambridge University Press

NEUMANN, J. & WENGLE, H. 2004 Coherent structures in controlled separated flow over sharp-edged and rounded steps. *J. Turbul.* **5**, 022.
NEW, T.H., LIM, T.T. & LUO, S.C. 2006 Effects of jet velocity profiles on a round jet in cross-flow. *Exp. Fluids* **40**, 859–875.
NISHINO, T., HAHN, S. & SHARIFF, K. 2010 Large-eddy simulations of a turbulent coanda jet on a circulation control airfoil. *Phys. Fluids* **22**, 125105.
PALUMBO, A., SEMERARO, O., ROBINET, J.-C. & LUCA DE, L. 2022 Boundary layer transition induced by low-speed synthetic jets. *Phys. Fluids* **34**, 124113.
PARK, H., JEON, W.-P., CHOI, H. & YOO, J.Y. 2007 Mixing enhancement behind a backward-facing step using tabs. *Phys. Fluids* **19**, 105103.
PERUMAL, A.K. & ZHOU, Y. 2018 Parametric study and scaling of jet manipulation using an unsteady minijet. *J. Fluid Mech.* **848**, 592–630.
PERUMAL, A.K., WU, Z., FAN, D.W. & ZHOU, Y. 2022 A hybrid artificial intelligence control of a turbulent jet: Reynolds number effect and scaling. *J. Fluid Mech.* **942**, A47.
PFINGSTEN, K.C. & RADESPIEL, R. 2009 Experimental and numerical investigation of a circulation control airfoil. *AIAA Paper* 2009-533
RAZZAGHI, M.J.P., MASOUMI, Y., SANI, S.M.R. & HUANG, G. 2022 Controlling flow separation over a curved ramp using vortex generator microjets. *Phys. Fluids* **34**, 115114.
RIZZETTA, D.P. & VISBAL, M.R. 2010 Large-eddy simulation of plasma-based turbulent boundary-layer separation control. *AIAA J.* **48**, 2793–2810.
SCIACCHITANO, A., WIENEKE, B. & SCARANO, F. 2013 Piv uncertainty quantification by image matching. *Meas. Sci. Technol.* **24**, 045302.
SELBY, G.V., LIN, J.C. & HOWARD, F.G. 1992 Control of low-speed turbulent separated flow using jet vortex generators. *Exp. Fluids* **12**, 394–400.
SELLERS, W.L., JONES, G.S. & MOORE, M.D. 2002 Flow control research at nasa langley in support of high-lift augmentation. *AIAA Paper* 2002-6006
SONG, S., DEGRAA, D.B. & EATON, J.K. 2000 Experimental study of a separating, reattaching, redeveloping flow over a smoothly contoured. *Int. J. Heat Fluid Fl.* **21**, 512–519.
SONG, S. & EATON, J.K. 2002 The effects of wall roughness on the separated flow over a smoothly contoured ramp. *Exp. Fluids* **33**, 38–46.
SONG, S. & EATON, J.K. 2004 Reynolds number effects on a turbulent boundary layer with separation, reattachment, and recovery. *Exp. Fluids* **36**, 246–258.
STELLA, F., MAZELLIER, N. & KOURTA, A. 2017 Scaling of separated shear layers: an investigation of mass entrainment. *J. Fluid Mech.* **826**, 851–887.
WARSOP, C. & CROWTHER, W.J. 2018 Fluidic flow control effectors for flight control. *AIAA J.* **56**, 3808–3824.
WEI, T., SCHMIDT, R. & MCMURTRY, P. 2005 Comment on the clauser chart method for determining the friction velocity. *Exp. Fluids* **38**, 695–699.
WONG, C., HALE, C., CHAN, B. & KONTIS, K. 2007 Experimental studies on steady and unsteady pneumatic trailing edge devices for subsonic flow applications. *AIAA Paper* 2007-1424
XU, H.Y., QIAO, C.L., YANG, H.Q. & YE, Z.Y. 2018 Active circulation control on the blunt trailing edge wind turbine airfoil. *AIAA J.* **56**, 554–570.
XU, K., SU, X., BENSOW, R. & KRAJNOVIC, S. 2022 Drag reduction of ship airflow using steady coanda effect. *Ocean Eng.* **266**, 113051.
ZHANG, S. & ZHONG, S. 2010 An experimental investigation of turbulent flow separation control by an array of synthetic jets. *AIAA Paper* 2010-4582
ZHANG, S. & ZHONG, S. 2011 Turbulent flow separation control over a two-dimensional ramp using synthetic jets. *AIAA J.* **49**, 2637–2649.
ZHANG, B.F., LIU, K., ZHOU, Y., TO, S. & TU, J.Y. 2018 Active drag reduction of a high-drag ahmed body based on steady blowing. *J. Fluid Mech.* **856**, 351–396.
ZHANG, X., WONG, C.W., CHENG, X.Q. & ZHOU, Y. 2022 Dependence of skin-friction reduction on the geometric parameters of blowing jet array. *Phys. Fluids* **34**, 105125.
ZHONG, S. & ZHANG, S. 2013 Further examination of the mechanism of round synthetic jets in delaying turbulent flow separation. *Flow Turbul. Combust* **91**, 177–208.

https://doi.org/10.1017/jfm.2025.10797 Published online by Cambridge University Press